







Spectral Units Analysis of Quadrangle H05-Hokusai on Mercury

F. Zambon¹ , C. Carli¹ , J. Wright² , D. A. Rothery², F. Altieri¹ ,
M. Massironi^{3,4} , F. Capaccioni¹, and G. Cremonese⁴ 

¹INAF-Istituto di Astrofisica e Planetologia Spaziali, Rome, Italy, ²The Open University, Milton Keynes, UK, ³Department of Geoscience, University of Padua, Padua, Italy, ⁴INAF - Osservatorio Astronomico di Padova, Padua, Italy

Key Points:

- H05 analysis reveals large spectral variabilities across the quadrangle
- We identified 11 spectral units, six large-scale and five local spectral units
- Comparison between morphostratigraphic and spectral units in some cases produce a good match

Correspondence to:

F. Zambon,
francesca.zambon@inaf.it

Citation:

Zambon, F., Carli, C., Wright, J., Rothery, D. A., Altieri, F., Massironi, M., et al. (2022). Spectral units analysis of quadrangle H05-Hokusai on Mercury. *Journal of Geophysical Research: Planets*, 127, e2021JE006918. <https://doi.org/10.1029/2021JE006918>

Received 9 APR 2021
Accepted 15 DEC 2021

Author Contributions:

Conceptualization: F. Zambon, C. Carli, J. Wright, D. A. Rothery, F. Altieri
Data curation: F. Zambon
Formal analysis: F. Zambon, C. Carli, F. Altieri
Funding acquisition: F. Altieri, M. Massironi
Investigation: F. Zambon, J. Wright, D. A. Rothery
Methodology: F. Zambon
Project Administration: F. Altieri, M. Massironi
Resources: F. Zambon
Software: F. Zambon
Supervision: F. Altieri
Validation: F. Zambon
Writing – original draft: F. Zambon
Writing – review & editing: F. Zambon, C. Carli, J. Wright, D. A. Rothery, F. Altieri, M. Massironi, F. Capaccioni, G. Cremonese

Abstract MESSENGER mission data allowed the entire surface of Mercury to be mapped at various spatial scales, from both geological and compositional stand points. Here, we present a spectral analysis of the H05-Hokusai quadrangle, using data acquired by the MESSENGER Mercury Dual Imaging System-Wide Angle Camera. We defined a suitable set of parameters, such as reflectance and spectral slopes, to study the spectral variation through the definition of spectral units. The determination of spectral units permits to infer the physical and compositional properties of a surface by processing several parameters simultaneously, instead of the more traditional approach of interpreting each single parameter separately. We identified 11 spectral units within H05, six large scale and five localized units. The large scale units include the northern smooth plains of Borealis Planitia. South-western H05 is characterized by two widespread spectral units, partially overlapping intercrater plains and intermediate plains. Furthermore, we found very localized spectral units corresponding to the low-reflectance blue material of Rachmaninoff basin and the high-reflectance red material of Nathair Facula. We investigated the link between spectral units and compositional maps obtained by GRS and XRS, to associate compositional information to the spectral units. We found some spectral units are correlated with Mg and Al variations displayed in the elemental maps. This implies that spectral variations associated to these units are mainly linked with composition rather than terrain maturity and/or grain size effects.

Plain Language Summary H05-Hokusai quadrangle, located on Mercury northern hemisphere, shows large spectral variations. In this paper, we analyzed the properties of H05 quadrangle considering the MESSENGER/MDIS-Wide Angle Camera data. To study the variability of H05, we defined 11 spectral units, useful not only for the spectral analysis, but also to lay the foundation for integrating spectral and morphostratigraphic information. Finally, to better characterize the geology of this quadrangle, we compared morphostratigraphic units and spectral units. We found a good match specially for few localized spectral units in correspondence of the low reflectance material of Rachmaninoff crater, Nathair facula, crater rays and ejecta. Furthermore, in some cases, spectral variations follow the Mg and Al variations derived by XRS. This confirms the spectral variations we observed in these specific areas, are mainly dominated by composition rather than other factors, such as grain size and/or terrain maturity.

1. Introduction

The recent MESSENGER mission (Solomon et al., 2007) substantially improved our understanding of planet Mercury (Solomon et al., 2018). Before MESSENGER, the only remote sensing data available were provided by the Mariner 10 mission (Giberson & Cunningham, 1975), and only 45% of Mercury's surface was imaged (Murray, 1975; Strom, 1979). MESSENGER Mercury Dual Imaging System (MDIS) covered the whole Mercury (Solomon et al., 2018). MDIS-Wide Angle Camera (MDIS-WAC) data reveal plentiful but subtle color variations, often associated with different terrain features (Denevi et al., 2009), and in some cases linked with compositional variations (Vander Kaaden et al., 2017; Vilas et al., 2016; Weider et al., 2015).

The MESSENGER X-ray (XRS) and Gamma Ray Spectrometers (GRS) observed variable amounts of several elements on Mercury's surface, enabling mapping of the global distribution of Mg and Al, and a partial coverage of other elements, such as Fe, S, Ca. Their contribution was fundamental to better constrain Mercury's composition. Based on these data, Weider et al. (2015) identified six different geochemical terranes, while Vander Kaaden et al. (2017) added three new terranes, lastly, Peplowski and Stockstill-Cahill (2019) found other two new

© 2022. The Authors.

This is an open access article under the terms of the [Creative Commons Attribution License](https://creativecommons.org/licenses/by/4.0/), which permits use, distribution and reproduction in any medium, provided the original work is properly cited.

terranes. A recent study by Nittler et al. (2020), improved the spatial resolution of previously published compositional maps (Weider et al., 2015) by 10%–15%.

For cartographic purposes, Mercury's surface is divided into 15 quadrangles (Figure 1). Morphostratigraphic maps based on Mariner 10 data covered all or part of only 9 of the 15 quadrangles, with a spatial scale of 1:5M (Davies, 1976). MESSENGER team members are working on a global morphostratigraphic map at a scale of 1:15M (Kinczyk et al., 2019).

Stand-alone 1:3M quadrangle geological maps, based on the MDIS data (Hawkins et al., 2007), have been made by Galluzzi et al. (2016); Mancinelli et al. (2016); Guzzetta et al. (2017); Wright et al. (2019). Other maps in the series are still being made, and in-progress versions of several have been presented at conferences (e.g., Galluzzi et al., 2018, 2019; Giacomini et al., 2018; Lewang et al., 2018; Malliband et al., 2018; Man et al., 2020; Pegg et al., 2018). These works are mainly focused on northern mid-latitude quadrangles, characterized by better MDIS-Narrow Angle Camera (NAC) and WAC spatial resolution data than more southerly region. A spectral analysis of the same quadrangles, covered by higher spatial resolution data, is in progress (see Bott et al., 2019; Carli et al., 2020; Ngoc et al., 2020).

Here we present a detailed spectral study of H05 quadrangle, located in Mercury's northern hemisphere (0°–90°E, 22.5°–65°N) based on MDIS-WAC data. This work follows the one published by Wright et al. (2019) focused on the identification of morphostratigraphic units and surface features across H05. The first goal of this paper is to carry out a spectral analysis of H05 by defining suitable spectral units (SUs) based on parameters that summarize the main spectral characteristics of the surface of Mercury. Since each SU encloses the information of all the spectral parameters selected, instead of considering a large number of maps, only two products are necessary for the final analysis, SUs and morphostratigraphic maps.

This approach not only simplify the interpretation, but help to search for a link between the morphostratigraphic units identified by Wright et al. (2019) and the SUs. Eventually, this work also lays the groundwork for the production of new integrated highly informative geological maps, where at each unit is associated both the morphostratigraphic and spectral/mineralogical information.

The integration of two different products, consolidated for terrestrial geological maps, is not largely applied to the other planetary bodies. Although several examples of morphostratigraphic (e.g., The Geology of Vesta, 2014;

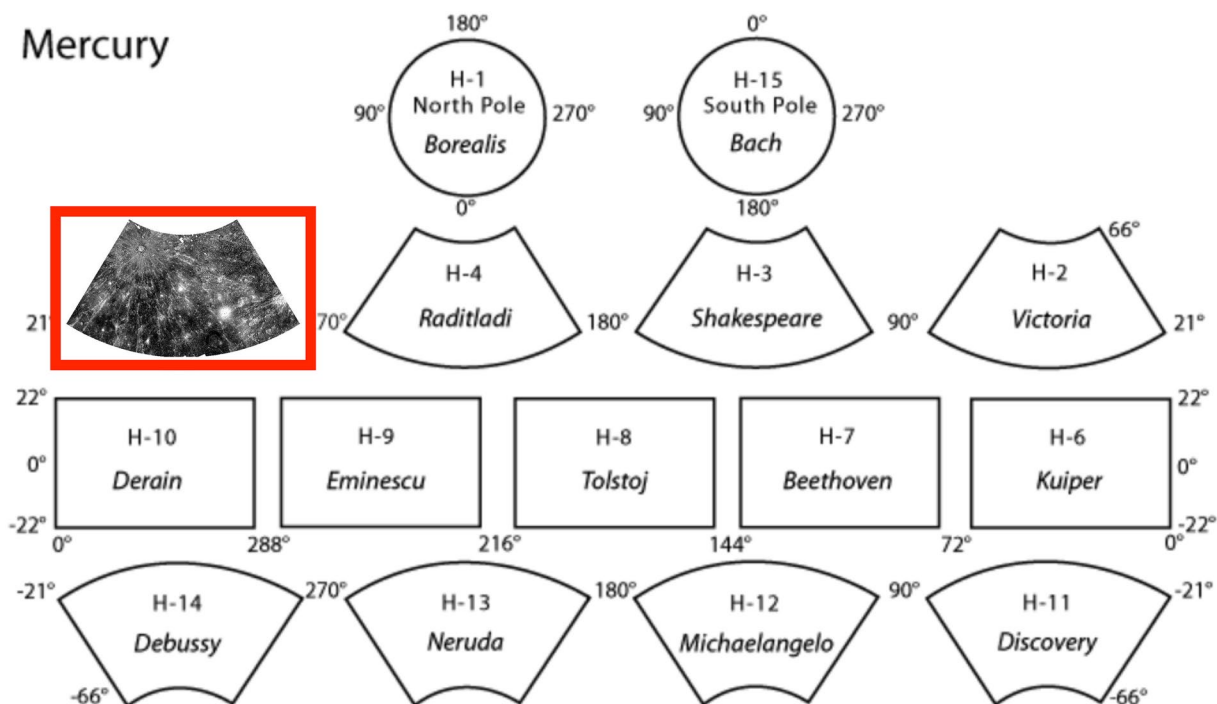


Figure 1. Mercury quadrangles division. Red box indicates H05-Hokusai quadrangle.

The geologic mapping of Ceres, (2018) and mineralogical maps (e.g., Vesta's Surface Composition, 2015; The Composition of Ceres, 2019) for some bodies are available, no integrated products are present. Integration of spectral, mineralogical or compositional maps with morphostratigraphic maps represents an evolution in the study of planetary surfaces, and improve the overall comprehension of the geological processes which characterized the different bodies of the Solar System.

2. Data Set and Data Processing

For this paper, we used the data acquired by MESSENGER/MDIS-WAC, and publicly available at the Mercury Orbital Data Explorer (ODE; <https://ode.rsl.wustl.edu/Mercury/>). Mercury global coverage is available for 8 of the 11 MDIS-WAC filters: *F* (433.2 nm), *C* (479.9 nm), *D* (558.9 nm), *E* (628.8 nm), *G* (748.7 nm), *L* (828.4 nm), *J* (898.8 nm), *I* (996.2 nm; Hawkins et al., 2007). Here we used the nominal wavelengths to refer the MDIS-WAC filters (see Denevi et al., 2018, Table 1).

We processed the 8 global coverage filters of H05 MDIS-WAC data using the Integrated Software for Imagers and Spectrometers (ISIS3.5.2; <https://isis.astrogeology.usgs.gov/Application/index.html>) and following the MESSENGER MDIS tutorial available in the Planetary Data System (PDS) website (<https://pds-imaging.jpl.nasa.gov/documentation/MESSENGERMDISWorkShopLPSC2103.pdf>).

The steps to create the 8-color reflectance mosaic of H05 are the following:

1. Among all the MDIS-WAC images including H05, we selected only those that can cover the quadrangle with all the 8 MDIS-WAC wavelengths (filters). For H05, we selected 502 multispectral cubes.
2. We calibrated the EDR (Experiment Data Record) images taking into account the calibration available in ISIS3.5.2 software and including: 1- dark current correction; 2- linearity correction; 3- readout smear correction; 4- uniformity (flat field) correction; 5- absolute coefficient correction; 6- conversion to irradiance over solar flux (*I/F*); 7- empirical correction (Denevi et al., 2018).
3. We applied the Kaasalainen-Shkuratov photometric correction model considering the parameters derived by Domingue et al. (2016). The images were normalized to standard photometric geometries of 30° incidence angle, 0° emission angle and 30° phase angle. To this purpose, we applied the Digital Elevation Model (DEM) provided by the Deutsches Zentrum für Luft und Raumfahrt (DLR) with a spatial resolution of 222 m/pixel (Preusker et al., 2017). This is the best DEM currently available, and it has been produced for only a few Mercury quadrangles, including H05 (<https://pds-imaging.jpl.nasa.gov/data/messenger/messdem1001/DEM/QUAD/IMG/>) (see Figure 2e). The application of this DEM is essential to accurately correct the local topographic effects in the high spatial resolution images.
4. We projected the photometrically corrected images onto an equirectangular map centered at 43.75°N and 45°. We selected the best spatial resolution images covering all the quadrangle, afterward we produced final maps with an average spatial resolution of 450 m/px.
5. We coregistered the images of each 8-filter set with respect to the *G* filter (750 nm).
6. We created the 8-filter cubes ordered by increasing wavelengths. The quadrangle mosaic is constructed with the mean value of the overlapping pixels for each filter.
7. Finally, we transformed the equirectangular 8-color mosaic into a Lambert conformal conic projection, the standard one for the mid-northern latitude quadrangles (center longitude: 45°E, standard parallel 1: 30°N, standard parallel 2: 58°N), in accordance with Wright et al. (2019).

3. Methods

We carried out the spectral analysis of Hokusai quadrangle using the 8-color mosaic obtained as described in Section 2. Starting from this mosaic, we produced color-composite maps to investigate variations associated with spectral variabilities. For a more in-depth analysis, we defined new spectral parameters, in addition to indices already known from the literature, such as spectral ratios and principal component analysis (see Blewett et al., 1997, 2007; Bott et al., 2019; Denevi et al., 2009). Starting from reflectance and these new indices, we finally define SUs.

Below, we describe in detail the spectral parameters and the RGB maps considered for this work (Figures 2 and 3).

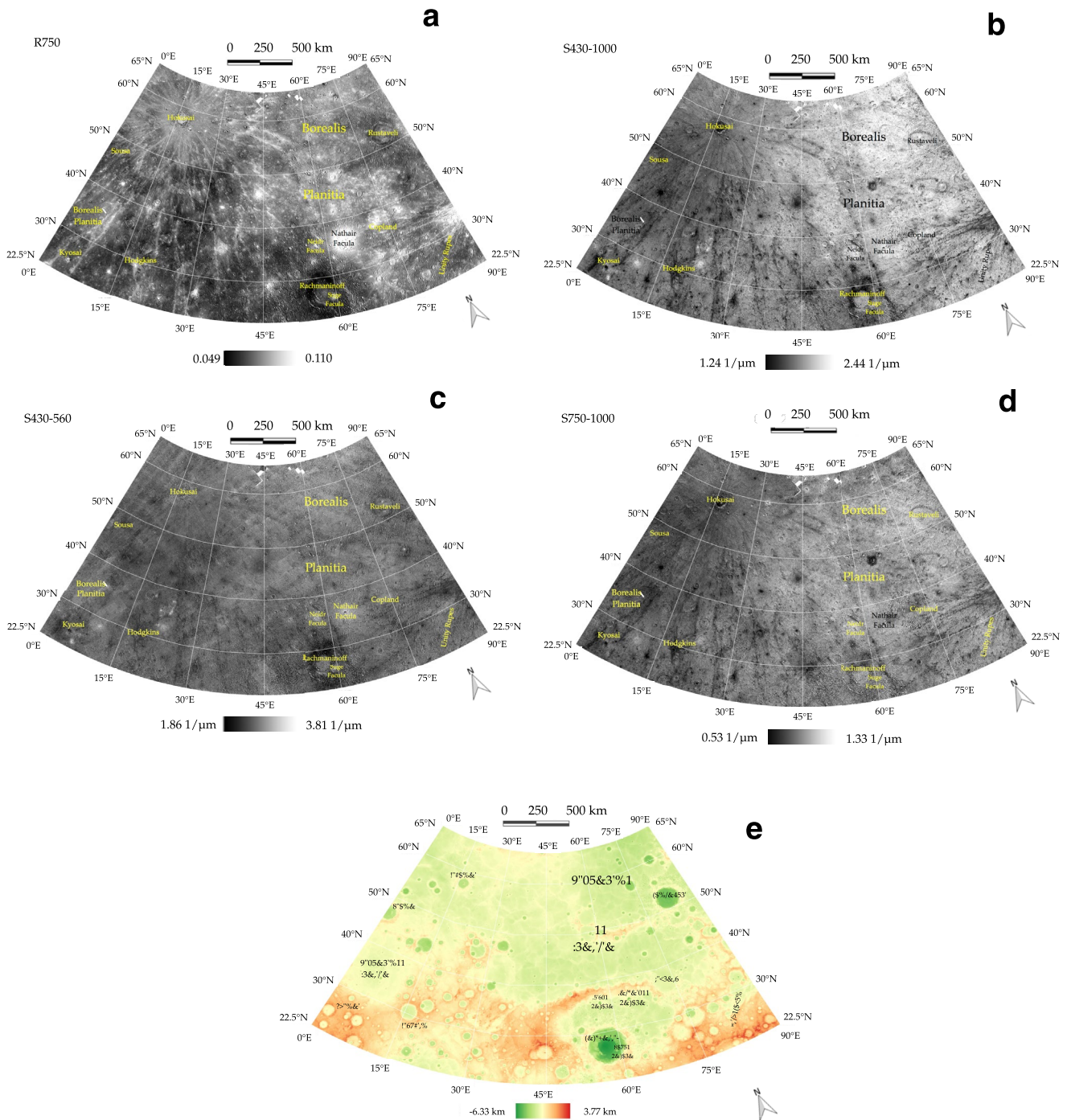


Figure 2. (a) Reflectance at 750 nm (R750 nm) map. (b) Map of the spectral slopes between 430 and 1000 nm, named global slope ($S_{430-1000}$). (c) Spectral slopes map calculated between 430 and 560 nm, indicated as $S_{430-560}$. (d) Map of the spectral slope between 750 and 1000 nm, called $S_{750-1000}$. (e) Hokusai topographic map, calculated with respect to the mean ellipsoid (radius 2439.4 Km) (Preusker et al., 2017).

3.1. Reflectance Map at 750 nm (R750)

Reflectance variations may indicate compositional diversities, variable particulate sizes, or surface roughness. This parameter can also highlight the presence of opaque mineral phases (e.g., oxide or carbon phases) and impact melts (Riner et al., 2009), as well as the degree of freshness or maturity of a terrain (Rava & Hapke, 1987). In particular, we have chosen the standard reflectance at 750 nm (G filter; Bott et al., 2019; Murchie et al., 2015)

Table 1
The Table Describes the Spectral Units Shown in Figure 5

Spectral unit	H05 spectral units				
	Spectral unit name	Spectral properties	Spectral parameters range	Compositional information	Associated morphostratigraphic unit
SU1	Very bright materials (VBM)	Very high R750 and very shallow $S_{750-1000}$ and $S_{430-1000}$ spectral slopes	R750: H-VH, $S_{430-560}$: IL-I $S_{750-1000}$: VL-L, $S_{430-1000}$: VL-L		Crater ejecta, crater wall, bright spots, very fresh material
SU2	Intermediate bright materials (IBM)	High R750 and shallow spectral slopes	R750: IH-H, $S_{430-560}$: L-I, $S_{750-1000}$: VL-IL, $S_{430-1000}$: L-IL		Crater rays, crater ejecta, bright spots, fresh material
SU3	Low bright materials (LBM)	Bright material with shallower spectral slopes than Hokusai average, but steeper than units #1, #2	R750: IH-H, $S_{430-560}$: L-I, $S_{750-1000}$: VL-L, $S_{430-1000}$: VL-L		Degraded rays and ejecta
SU4	Rachmaninoff dark materials (RDM)	Very low R750, very shallow $S_{430-560}$ and $S_{430-1000}$, shallow $S_{750-1000}$	R750: VL-L, $S_{430-560}$: VL-LI, $S_{750-1000}$: VL-IL, $S_{430-1000}$: VL-L	H Mg, IL Al	Floor of Rachmaninoff basin annulus
SU5	Intermediate units (IU)	Intermediate values of all the spectral parameters	R750: VL-IL, $S_{430-560}$: I-IH, $S_{750-1000}$: I-H, $S_{430-1000}$: I-H	east Borealis Planitia-nsp: IH Mg, IL Al	Cratered terrains
SU6	High reflectance and spectral slopes units (HRSU)	High reflectance and steep spectral slopes	R750: IL-IH, $S_{430-560}$: IH-VH, $S_{750-1000}$: I-H, $S_{430-1000}$: I-H	nsp: I Mg and Al	Faculae and Borealis Planitia
SU7	Nathair Facula (Nat)	Very high reflectance and very steep spectral slopes	R750: H-VH, $S_{430-560}$: H-VH, $S_{750-1000}$: I-IH, $S_{430-1000}$: I-IH	IH Mg, L Al, H Ca, L S	Nathair Facula
SU8	Intermediate dark material (IDM)	Intermediate low R750, shallow spectral slopes	R750: IL-I, $S_{430-560}$: L-I, $S_{750-1000}$: L-I, $S_{430-1000}$: VL-IL		Intermediate terrains
SU9	Intermediate material low spectral slopes (IMLS)	Intermediate-high R750 and intermediate low $S_{430-560}$ and $S_{430-1000}$	R750: I-H, $S_{430-560}$: IL-IH, $S_{750-1000}$: L-I, $S_{430-1000}$: L-I	Hokusai rays in BP-nsp: IH Mg, IL Al Bright crater (35.25°E, 35.46°N): H Al, L Mg	Hokusai ejecta
SU10	Dark material low spectral slope (DMLS)	Very low-low R750, shallow spectral slopes	R750: VL-L, $S_{430-560}$: L-I, $S_{750-1000}$: L-I, $S_{430-1000}$: L-I		Low reflectance intermediate terrains
SU11	Low reflectance material, high spectral slopes (LRHS)	Low R750, intermediate high-very, high spectral slopes	R750: VL-IL, $S_{430-560}$: IH-VH, $S_{750-1000}$: IH-VH, $S_{430-1000}$: IH-VH		Low reflectance Borealis Planitia
SU12	Unclassified pixels unit (UP)	All the regions not included in the previous units. Mainly regions affected by photometric artifacts.			

Note. The authors indicate with VH, H, IH, I, IL, L and VL, very high, high, intermediate high, intermediate, low and very low values of the spectral parameters, compared with H05 average. The spectral parameters range of values for each single parameter are reported in Appendix A.

from the H05 8-color mosaic (Figure 2a). R750 can be useful for identifying morphological units and surface structures, but a more in-depth study can be done investigating the correlation between reflectance and other spectral indices, such as spectral slopes (see Section 3.2). Scatter plot 2D of spectral slopes versus reflectance enables discrimination of areas with different spectral characteristics, often associated with specific terrains (e.g., opaque materials show lower reflectance at 750 nm and shallower spectral slopes, while bright regions display higher reflectance and lower spectral slopes values than the average of Mercury; see Figure 4a, Blewett et al., 2007 and Blewett et al., 2009).

3.2. Spectral Slopes

Spectral slope is related to several factors, such as composition, grain size, terrain maturity, and space weathering (Noble & Pieters, 2003; Pieters & Noble, 2016). Spectral slopes are the main investigative tool when the spectra of a surface lack clear absorption bands, as is the case of Mercury at the spatial scale of MDIS. To calculate spectral slopes, we used the method of Cuzzi et al. (2009); and Filacchione et al. (2012):

$$S_{\lambda_1, \lambda_2} = \frac{R_{\lambda_2} - R_{\lambda_1}}{(\lambda_2 - \lambda_1)R_{\lambda_1}}$$

where λ_1 and λ_2 are the extremes of the range of wavelengths considered, R_{λ_1} and R_{λ_2} the reflectance at λ_1 and λ_2 respectively. We normalized spectral slopes by R_{λ_1} to remove possible reflectance and solar phase dependencies.

Airless silicate bodies, such as the Moon and Mercury, generally exhibit an increase in spectral slope with age (spectral reddening) especially in the visible/near infrared range (VIS/NIR), mainly due to the exposure to the space environment (Denevi et al., 2014; Lucey & Riner, 2011; Noble & Pieters, 2003; Pieters et al., 2000). To analyze H05 quadrangle, we considered three different spectral slopes: the MDIS-WAC global slope ($S_{430-1000}$) between 430 and 1000 nm, to study the overall variations; the spectral slope between 430 and 560 nm ($S_{430-560}$), useful for the detection of opaque mineral phases and volcanic origin materials (Blewett et al., 1997, 2007); and the slope between 750 and 1000 nm ($S_{750-1000}$) sensitive to the possible presence of absorptions around 1 μm (Thangjam et al., 2013).

1. **Spectral slope between 430 and 1000 nm, or global slope ($S_{430-1000}$)**—On Mercury, $S_{430-1000}$ (Figure 2b) is useful to study terrain maturity, which is often linked to space weathering effects (Noble & Pieters, 2003). $S_{430-1000}$ is a powerful parameter to identify bright fresh ejecta. Young fresh materials and crater ray materials display shallower values of this index (“blue slopes”), whereas steep spectral slopes (“red slopes”) are typical of mature terrains.
2. **Spectral slope between 430 and 560 nm ($S_{430-560}$)**—The spectral range close to ultraviolet/visible (UV/VIS) has been used to identify dark material on the Moon (Clark et al., 1986). On Mercury, $S_{430-560}$ together with the reflectance, is useful for distinguishing opaque mineral phases (Blewett et al., 1997, 2007) associated with low reflectance material (LRM; Denevi & Robinson, 2008; Klima et al., 2018) from other terrains. In addition, $S_{430-560}$ is particularly worthwhile for picking out regions with volcanic origin, for example, Borealis Planitia and faculae whose spectra appear redder than those of other regions in this range of wavelengths (Figure 2c).
3. **Spectral slope between 750 and 1000 nm ($S_{750-1000}$)**—Many mafic minerals have a 1 μm absorption band. Negative or low $S_{750-1000}$ values (Figure 2d) could indicate the possible presence of this absorption feature (Thangjam et al., 2013). The 1 μm band could be caused primarily by the presence of Fe^{2+} and could thus give a constraint for identifying or distinguishing specific mineralogical phases, such as pyroxene, olivine, plagioclase (Burns, 1993) or glasses (Adams & McCord, 1971), even though other iron-bearing minerals can show an absorption attributed to Fe^{2+} in this spectral region (e.g., chromite (Cloutis et al., 2004), iron oxide hematite (Clark, 1999)). Furthermore, when iron abundance is very low, other transition elements could be present (e.g., Ti in oxides and silicates or glasses; Burns, 1993; Pieters & Tompkins, 2005). In addition other elements, such as Ni in mafic minerals, could also be responsible for the 1 μm absorption feature (Burns, 1993).

3.3. Color Composite Mosaics and Morphostratigraphic Map

Color composite mosaics are a powerful tool to investigate spectral variations of a surface, where ideally each color could correspond to a variation in composition. Below, we describe the color composite combinations already used by other authors (Denevi et al., 2009), and a new RGB color mosaic introduced here for the first time.

1. RGB ‘false color’ mosaic (R: 1000 nm, G: 750 nm, B: 430 nm) - This particular combination is analogous to natural color, except that it spans a wider range of wavelengths, therefore we refer to it here as a “false” color mosaic. It emphasizes reflectance and color variations (Figure 3a) across the quadrangle. In common with a widespread practice, we assign the wavelength closest to the near infrared (NIR; 1000 nm) to the red channel, the intermediate one (750 nm) to the green channel, and the one closest to the ultraviolet-visible (UV/VIS; 430 nm) to the blue channel. This color combination facilitates association of the color of a region with wavelengths, from UV/VIS to VIS/NIR. Unlike blue areas, redder regions are associated with higher reflectance at longer wavelengths.
2. RGB ‘Enhanced Color Mosaic’ (R: PC2, G: PC1, B: R430 nm/R1000 nm) - This RGB color combination is the principal one considered by the MESSENGER team to better highlight differences in composition on Mercury surface (Denevi et al., 2009; Robinson et al., 2008), and it is based on a Principal Component Analysis (PCA; Wold et al. (1987)). PC2 is displayed in the red channel, PC1 in the green channel, and a ratio of spectral reflectances R430/R1000 nm in the blue channel. PCA is a good tool for discriminating variations within a given data set (Wold et al., 1987), although it is strictly dependent on the region and the set of parameters considered. We applied PCA to the Hokusai 8-color mosaic and we show the result in Figure 3b. PC1 is indicative of reflectance differences, while PC2 is linked to spectral variations not due to reflectance (e.g., spectral slopes variability) and largely removes the spectral effects of maturity (Denevi et al., 2009). The ratio R430/R1000 nm takes into account the global spectral slope variations. In this way, red and blue channels are linked with compositional variations, and green channel with maturity variations, highlighting fresh material (Denevi et al., 2009).
3. RGB “Clementine-like Color Mosaic” (R: R750 nm/R430 nm, G: R750 nm/R1000 nm, B: R430 nm/R750 nm) - This RGB color combination was originally defined for the Moon using Clementine camera data and is worthwhile to identify mafic minerals, glassy phases, low- and high-titanium regions (Lucey et al., 2000; Pieters et al., 1994). Mercury’s surface has somewhat different characteristics because of differences in mafic composition and in space weathering processes, but nevertheless this color combination helps to highlight compositional variations associated with morphostratigraphic units. The western side of H05, including part of Borealis Planitia-northern smooth plains, and faculae appear red/orange in this color combination, while the eastern part of the quadrangle dominated by Hokusai rays and ejecta and Rachmaninoff basin-LRM display a blue/light blue color (Figure 3c).
4. RGB “Spectral Slope Color Composite Mosaic” (R: $S_{430-1000}$, G: $S_{750-1000}$, B: $S_{430-560}$) - The spectral slope color combination summarizes in one map the spectral slope variation described in Section 3.2 (Figure 3d). This simplifies discrimination of the spectral slopes variability of a given region.
5. Morphostratigraphic map - To aid our analysis, we considered the morphostratigraphic map of H05 published by Wright et al. (2019) (Figure 3e). Wright et al. (2019) mapped several units: northern smooth plains of Borealis Planitia (Borealis Planitia-nsp) and other smooth plains (sp), intercrater plains (icp), intermediate plains (ip), and crater materials classified by degradation state. Icp was probably emplaced by effusive volcanism during Pre-Tolstojan or Tolstojan times (older than about 3.8 Ga), but has become densely cratered. The more recent sp unit (early Calorian) is believed to a less-cratered equivalent of icp that has retained clear evidence of its effusive origin such as wrinkle ridges and lava-flooded ghost craters, whereas ip has intermediate morphological characteristics (Figure 3e).

Wright et al. (2019) also mapped superficial features, such as crater rays, widespread across the quadrangle and faculae, often associated with putative explosive volcanic vents. In Figure 3f, we show the distribution of the H05 morphostratigraphic units. Wright et al. (2019) produced two versions of the H05 morphostratigraphic map, one following the crater material three-class system (c1, c2, c3), in accordance with Mancinelli et al. (2016); Galluzzi et al. (2016); Guzzetta et al. (2017), and a parallel map using a five-class system (c1, c2, c3, c4, c5), based on classification introduced after Mariner 10 and still in use for the global morphostratigraphic map of Mercury (e.g., Kinczyk et al., 2020). Each crater material classification c1-c3 and c1-c5 is ranked by decreasing degradation state, with c3 or c5 being craters that have retained the most pristine morphology. Here, we consider only the simpler c1-c3 classification, as used in the large scale maps of Mancinelli et al. (2016); Galluzzi et al. (2016); Guzzetta

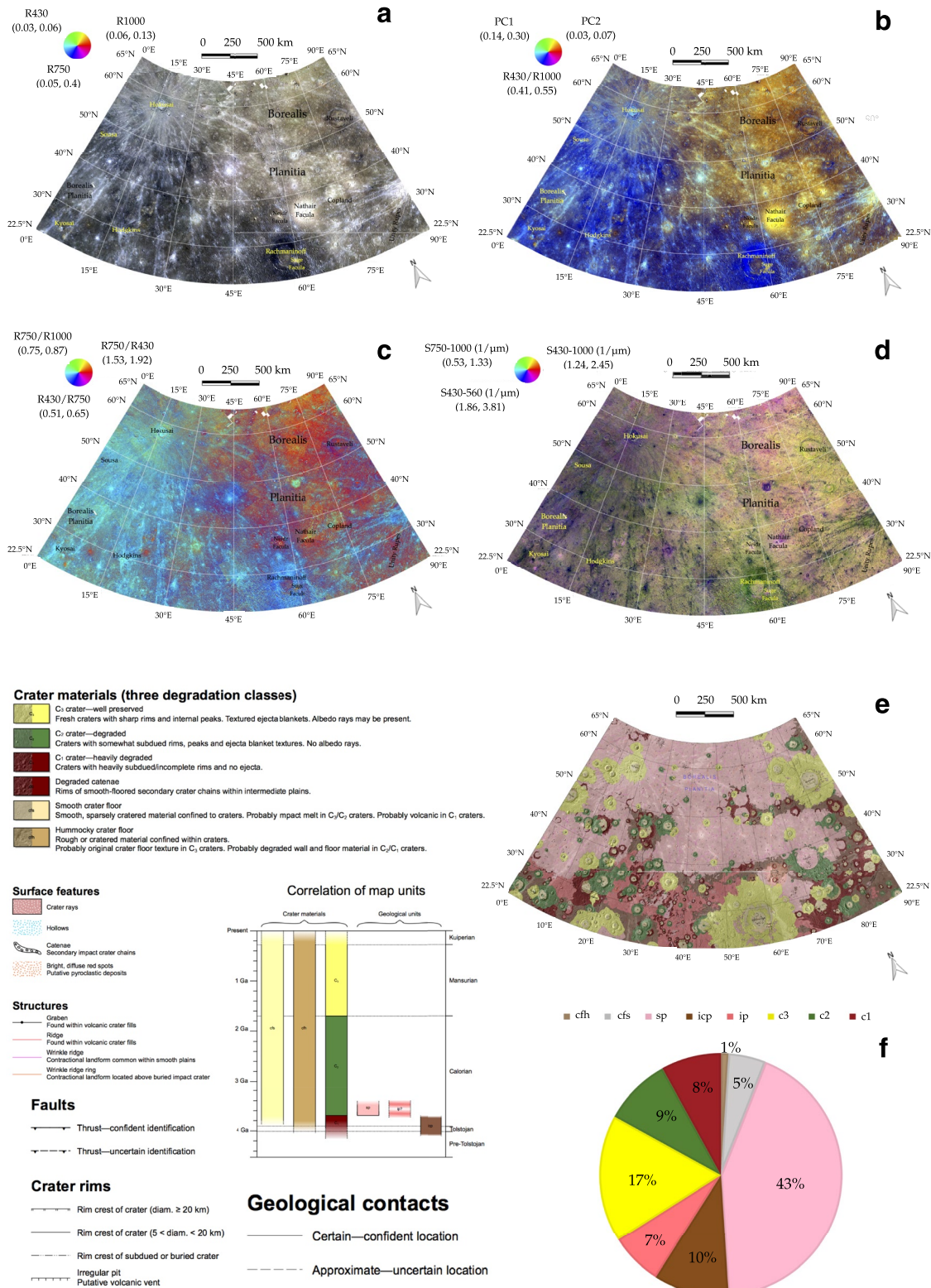


Figure 3.

et al. (2017); Wright et al. (2019). Craters with visible rays are the most recent and belong to the Kuiperian system ($<280 \pm 60$ Ma), according to Banks et al., (2017), while other fresh, well-preserved (c3) craters, which have lost their rays, are typical of the Mansurian system (1.7–0.28 Ga, see Banks et al., 2017). Space weathering processes have erased the traces of bright ejecta in the older craters (\sim c2) dating from the Calorian (<3.8 Ga, Ernst et al., 2017), Tolstojan and Pre-Tolstojan (\sim c1, 3.8–3.9 Ga and >3.9 Ga, Ernst et al., 2017; Figure 3e). Fresh, less degraded craters (c3) superimpose all plains types, while the most degraded crater (c2 and c1) are mainly in icp and ip (Figure 3e). The topographic map in Figure 2e, shows a clear division between the northern part of the quadrangle covered by Borealis Planitia-nsp and the southern side, where icp and ip dominate. The elevation differences span between -6.33 km and $+3.77$ km relative to the mean ellipsoid. Rachmaninoff and Rustaveli craters record the lowest elevations (Zuber et al., 2012), whereas icp and ip tend to be at the highest elevations in this quadrangle.

3.4. Spectral Units Definition

We exploit the spectral indices described in Sections 3.1 and 3.2 to identify SUs for H05. SUs provide a powerful tool to evaluate the spectral characteristics of a surface. They convey at the same time the spectral information carried by a selected set of parameters, facilitating the understanding of the spectral properties of a surface. SUs are characterized by specific interval of values for the spectral parameters, therefore, they yield the spectral properties of a given region.

To retrieve the SUs for H05, we considered a subset of the most representative parameters: R_{750} , $S_{430-560}$, $S_{750-1000}$ and $S_{430-1000}$ (see Sections 3.1 and 3.2). We defined the SUs thresholding each spectral parameter range of values in seven intervals: very low (VL), low (L), intermediate low (IL), intermediate (I), intermediate high (IH), high (H) and very high (VH) values.

The maximum number of threshold intervals depends on the computation time and on the number of combination of intervals. A large number of spectral parameters combined with too many threshold intervals, would increase excessively the spectral units, which must be merged in a second moment. Hence, after the identification of the most relevant spectral indices, it is necessary to define the number of threshold intervals, which varies based on the surface and on the histogram distribution of the spectral parameters values. After an accurate analysis of H05 spectral indices, we found the proper number of threshold intervals for each parameter is seven.

To define the threshold values, we calculated the main statistical parameters (mean, standard deviation, median, mode, maximum and minimum values of the distribution). A first attempt to define the SUs was made by considering the mean value of each parameter and identifying threshold intervals of the same length, as multiple of the standard deviation. Afterward, we considered similar automatic methods, using as reference value the mode and the median of the distribution, instead of the mean. However, we realized that an automatic threshold intervals definition does not take into account the characteristics of the indices distribution, assigning regions with different spectral characteristics to the same unit.

Therefore, the best choice was the application of a semi-automatic method, where, in addition to the histogram of the parameters values, we considered the 2D density scatter plots of the spectral indices. This allows both to highlight homogeneous clusters and to consider the density of the distribution of the parameters values, permitting to identify and assign regions with similar spectral characteristics to the same SU (see Figures A1 and A2 in Appendix A).

Subsequently, we applied all the possible combinations of the threshold intervals for the four selected parameters, and we merged together units with spectral indexes having close values ($<10\%$) and containing only a reduced number of pixels ($<10^5$), obtaining eventually the 11 final SUs for H05.

Threshold intervals maps and values are reported in Appendix A.

Figure 3. (a) Hokusai quadrangle RGB “false color” mosaic: R: 1000 nm, G: 750 nm, B: 430 nm. (b) RGB color composite mosaic, called “enhanced color” mosaic, R: PC2, G: PC1, B: 430/1000 nm. (c) RGB “Clementine-like” color composite mosaic, color assignments are similar to those used for the Clementine maps of the Moon (Pieters et al., 1994): R: R (750 nm)/R (430 nm), G: R (750 nm)/R (1000 nm), and B: R (430 nm)/R (750 nm). (d) H05 RGB “spectral slopes color composite mosaic”: R: $S_{430-1000}$, G: $S_{750-1000}$, B: $S_{430-560}$. (e) Hokusai morphostratigraphic map produced by Wright et al. (2019). (f) Distribution of the morphostratigraphic units across Hokusai quadrangle shown in panel (e).

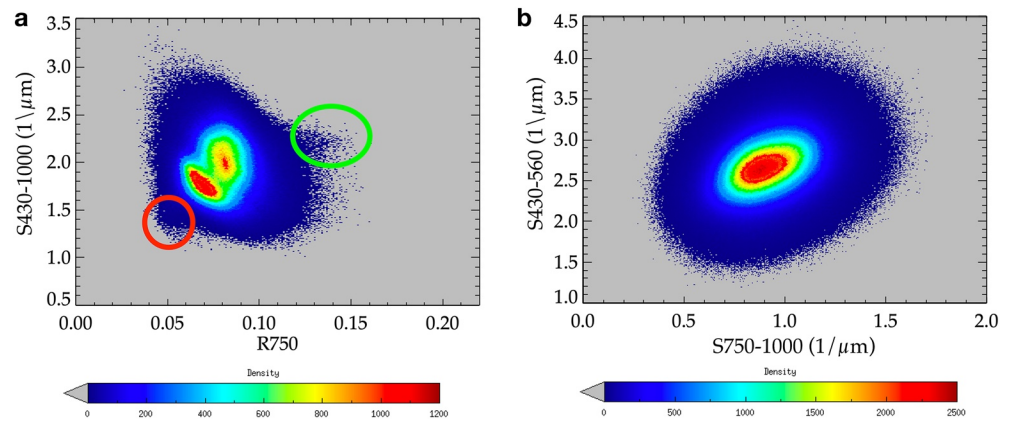


Figure 4. (a) Global slope versus reflectance at 750 nm density scatter plot. Red circle indicates Rachmaninoff basin-low reflectance material, while green circle Nathair Facula. (b) $S_{430-560}$ versus $S_{750-1000}$ density scatter plot.

In Figures 4a and 4b, we display an example of density scatter plots for $S_{430-1000}$ versus R_{750} and $S_{430-560}$ versus $S_{750-1000}$. The $S_{430-1000}$ versus R_{750} plot shows a bimodal distribution in the central bulk, reflecting the quadrangle's east-west dichotomy of H05, linked with Borealis Planitia-nsp and Hokusai ejecta superposing the northern smooth plains in the western side of the quadrangle. The regions enclosed in the red and green circles of Figure 4a highlight Rachmaninoff basin-LRM (red circle) and Nathair Facula (green circle) units. The bimodal distribution disappears when we consider the $S_{430-560}$ versus $S_{750-1000}$ plot (Figure 4b).

The SUs obtained for Hokusai quadrangle are shown in Figure 5. In Table 1, we describe the characteristics of each SU.

4. Morphological and Spectral Variability Across H05

H05 is a quadrangle containing much variety, from morphological and spectral point of view. The map in Figure 2a highlights considerable reflectance variations, emphasizing different terrains and surface features.

Starting from the morphostratigraphic map of H05 produced by Wright et al. (2019), we calculate that icp and ip cover $\sim 17\%$ of the surface of the entire quadrangle (Figure 3f). These terrains dominate the southern part of H05 and appear darker and bluer in the false color RGB map, indicating a major reflectance contribution at shorter wavelengths. This is also emphasized in the enhanced mosaic (Figure 3b).

Very dark LRM is visible in the floor of the annulus of the Rachmaninoff basin (Figure 2a; see Section 5.2.2). Despite its low reflectance, this region shows spectral slopes behavior similar to bright crater rays and ejecta. The shallow spectral slopes of Rachmaninoff basin-LRM, especially in the UV-VIS region, is a typical characteristic of opaque mineralogical phases (Blewett et al., 1997), suggesting the composition dominates this area. In contrast, although the low spectral slope values for the bright crater materials (Figures 2b–2d) could be related to composition, this is likely the result of less space weathering exposure, due to the young age of these features.

Borealis Planitia-nsp occupies 43% of the surface of H05 (Figure 3f). Denevi et al. (2013) mapped smooth plains (sp) across the entire planet. They found 27% of Mercury's surface is covered by sp, largely distributed in the northern hemisphere, where most of it corresponds to Borealis Planitia-nsp. Albeit the whole northern part of the quadrangle was mapped as Borealis Planitia-nsp by Wright et al. (2019), RGB maps in Figures 3a–3c, show a clear spectral dichotomy between the eastern and western side of H05. The eastern part of the quadrangle displays the typical behavior of the Borealis Planitia-nsp, showing high values of reflectance and spectral slopes, especially in the UV-VIS and the global spectral range. In the western side of H05, Hokusai ejecta overlay Borealis Planitia-nsp, influencing the spectral characteristics of this region (Figures 2a–2d). Borealis Planitia-nsp show reflectance values up to 8% higher than those of icp and ip (Figure 2a), and spectral slopes $\sim 4\%$ steeper in the UV-VIS range (Figure 2c). This contrast is particularly evident in the enhanced color mosaic (Figure 3b), where Borealis Planitia-nsp are yellow-orange and icp and ip are blue.

Spectral Units

a

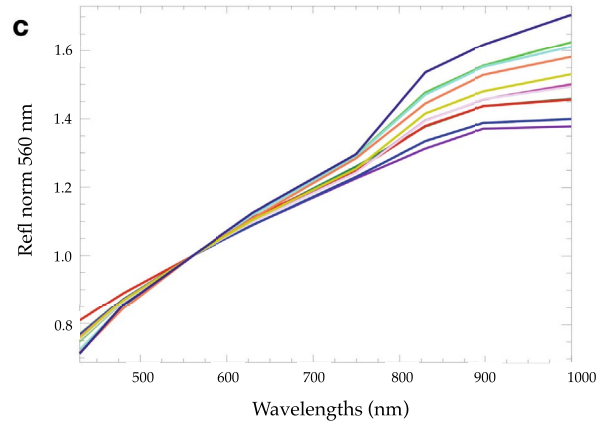
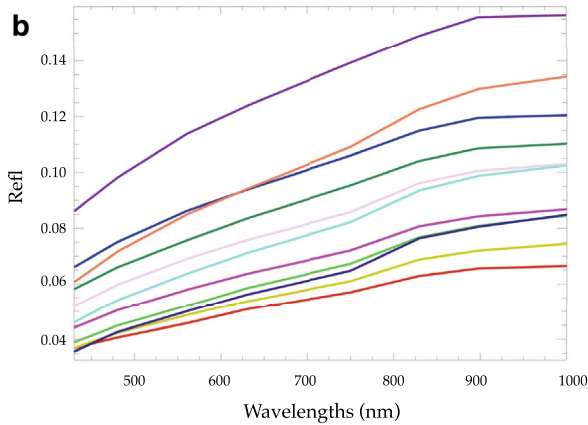
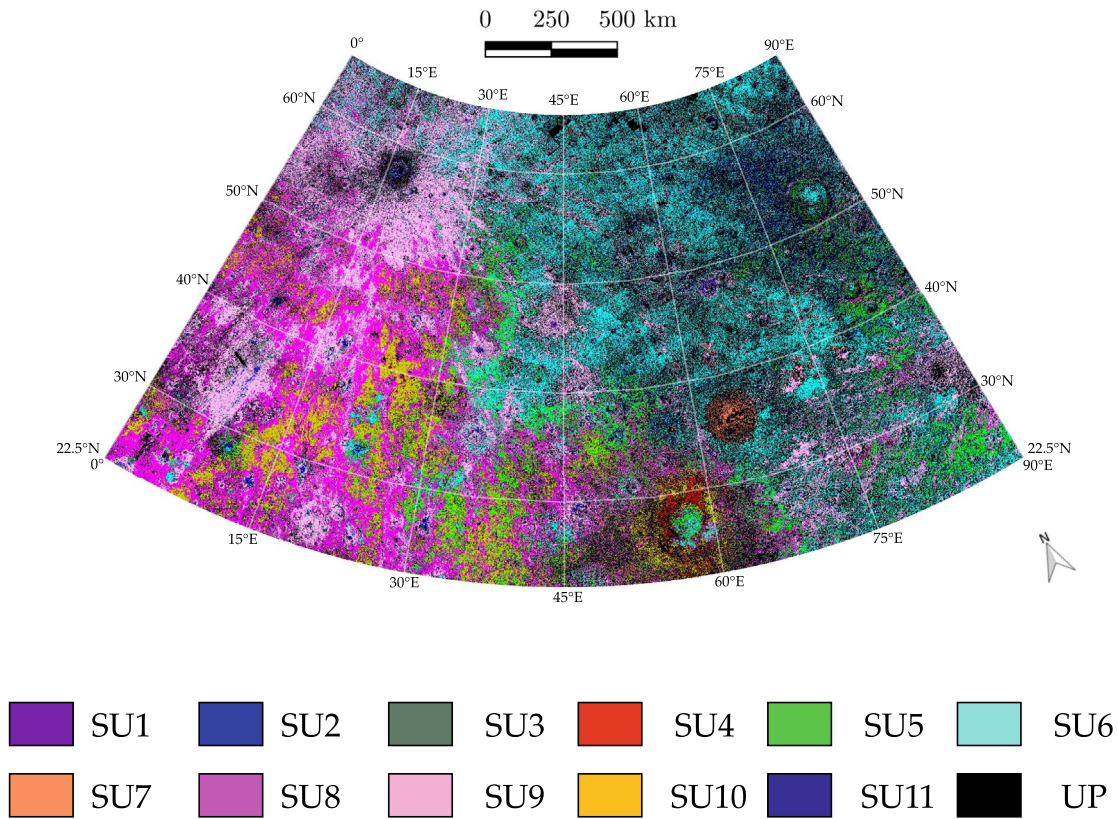


Figure 5. (a) Spectral units map of Hokusai quadrangle. (b) Average reflectance spectra of the spectral units shown in panel (a). (c) Same spectra of panel (b) normalized at 560 nm. Color of the spectra are consistent with the color of the units displayed in panel (a). The characteristics of the spectral units are summarized in Tables 1 and 2.

The high reflectance and spectral slopes values of Borealis Planitia-nsf probably are related to composition rather than space weathering. Space weathering increases spectral slopes, decreasing the albedo (Noble & Pieters, 2003), which is not observed in the Borealis Planitia-nsf. Furthermore, Borealis Planitia-nsf are dated to the early Calorian, between 3.8 and 3.4 Ga, and are younger than icp, which they clearly superpose. For these

reasons, we can infer the composition plays a major role in the spectral distinction between Borealis Planitia-nsp and icp.

H05 is also characterized by the presence of several faculae, often hosting vents and generally associated with volcanic pyroclastic deposits (Goudge et al., 2014; Thomas et al., 2014a, 2014b). These features have spectral characteristics similar to Borealis Planitia-nsp, but a common origin is unlikely because of the clear differences in emplacement style.

A comparison between Hokusai quadrangle and Mercury global mean spectra, reveals that reflectance is 10% higher for H05 (Figure 6a), with an enhancement of 6.4% in spectral reddening (Figure 6b). These differences are due to the large extent of the Borealis Planitia-nsp, and the presence of Nathair Facula and other faculae in H05.

H05 also exhibits a number of c3 craters (Wright et al., 2019), covering 17% of surface of the quadrangle (Figure 3f). H05 is largely dominated by the rays of Hokusai and Fonteyn craters and by the ejecta of several impact craters (Figure 3b). Hokusai crater, with its widespread ray system, is one of the freshest large craters on Mercury (Barnouin et al., 2015), while Fonteyn ($D = 29$ km, 32.82°N , 95.51°E) is a smaller crater in the adjacent H04 quadrangle, whose rays extend into H05. Fresh bright crater rays and ejecta, spectrally bluer than the other regions, stand out in Figure 2b.

Due to their spectral characteristics and size, at the spatial scale of our maps, we are not able to identify a specific SU for hollows. Hollows are small depressions formed where volatiles have been lost from the surface (Blewett et al., 2007, 2011, 2013, 2016; Thomas et al., 2016). Hollows have peculiar spectral characteristics, in some cases, for example, Dominici crater, they show an absorption band at 600 nm (Lucchetti et al., 2018; Vilas et al., 2016). In H05, few hollows are present, mainly distributed in the southern part of the quadrangle, while they are identified only in one region in Borealis Planitia-nsp, within Rustaveli crater floor.

5. Spectral Units of Hokusai Quadrangle

For H05, we found 11 SUs (Figure 5). We identified six large scale units (SU5, SU6, SU8, SU9, SU10, SU11), each one, except SU10 and SU11, covers more than 15% of H05, conversely the localized units (SU1, SU2, SU3, SU4, SU7) occupy only few % of the surface of the quadrangle. The unclassified pixels unit (UP), widespread in the whole H05, represents ~37% of the quadrangle. UP includes regions with not optimal illumination condition, such as craters edges and rims, and areas affected by photometric residuals.

The large scale units cover large areas extended overall the quadrangle, while others units are located in correspondence with some morphological features. SUs have a good match with the morphostratigraphic units shown in Figure 3e, only in a few cases. We observe a good correlation with localized units, for example, Nathair Facula (SU7), Rachmaninoff basin-LRM (SU4) and some crater rays and ejecta (SU1, SU2, SU3), and with the large scale unit linked with Hokusai crater ejecta (SU9). The area of SU7 covering Nathair Facula, is almost coincident

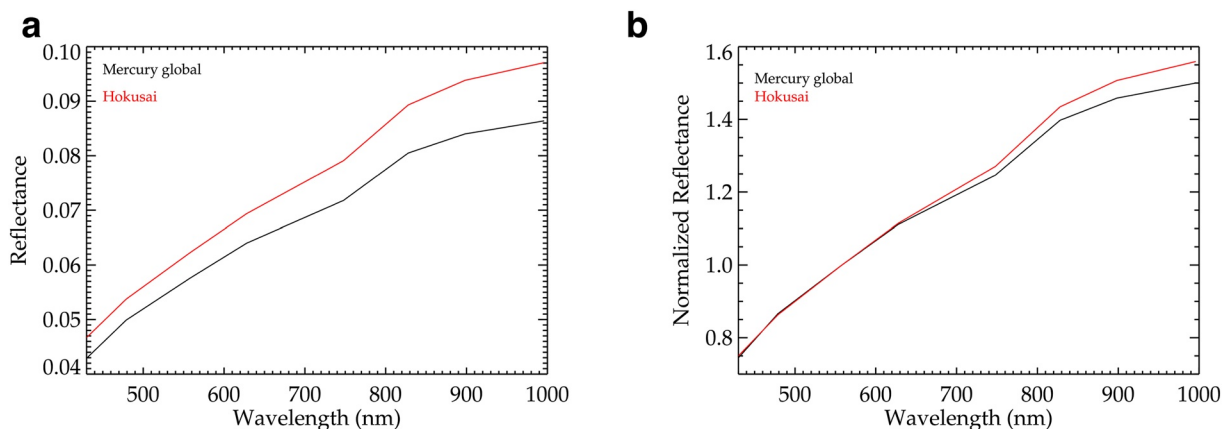


Figure 6. (a) Mercury average spectrum obtained by the USGS MDIS global 8-color map (<https://messenger.jhuapl.edu/>) (black), compared with Hokusai average spectrum (red). (b) Same plot shown in (a) normalized at 560 nm.

and is entirely included in the same surface feature in the morphostratigraphic map (Figure 3e). The ratio between Nathair Facula area in SU7 and in the morphostratigraphic map, is 0.9. Likewise, the same ratio for Rachmaninoff basin-LRM area and SU4 is 1.05. SU1, SU2, SU3 are included in the corresponding morphological units, showing a similar extension.

The widespread SUs do not belong entirely to any morphological unit. For example, SU6 covers almost half of the sp (areas ratio ~ 0.47), while the rest of the sp contains part of other SUs.

Below we describe in detail the SUs belonging to large and local scale units.

5.1. Large Scale Spectral Units

The six large scale units (SU5, SU6, SU8, SU9, SU10 and SU11) are all included or partially included in Borealis Planitia-nsp unit identified in the morphostratigraphic map by Wright et al. (2019). In the eastern side of H05, less affected by the ejecta and rays from Hokusai crater, we identified two units SU6 and SU11 associated with Rustaveli crater and its ejecta. SU11 has lower reflectance than SU6, but steeper spectral slopes. The western side of H05, where the ejecta and rays of Hokusai crater superimpose Borealis Planitia-nsp, is dominated by SU9. SU9, is the most widespread unit, covering more than 16% of the quadrangle, it has intermediate high R750 and intermediate low $S_{430-560}$ and $S_{430-1000}$ values. Fonteyn crater rays, in the eastern side of H05, show spectral characteristics similar to Hokusai rays, and are included with those in SU9.

SU5 has intermediate values of the spectral parameters. It separates the eastern and western side of Borealis Planitia-nsp, and is also present in the south-eastern part of the quadrangle. SU10 corresponds to very low to low R750, and shallow spectral slopes. This unit partially overlaps icp and ip. SU8, largely distributed in the south-western side of the quadrangle, surrounds SU9. This unit has intermediate R750 values and shallow spectral slopes. The reflectance and spectral slopes of SU8 suggest that it is a unit intermediate between SU9 and SU10, which is likely the result of the mixing between Hokusai rays material and icp/ip terrain units.

The different SUs within the Borealis Planitia-nsp, indicate a large spectral variability across the northern region of H05, not observed in the morphostratigraphic map, where Borealis Planitia-nsp are mapped in an unique morphological unit.

To better constrain the compositional properties of the SUs, we considered the elemental maps from XRS and GRS (Nittler et al., 2020; Weider et al., 2015) for H05 (see Figure 7). SU5 and SU6 are characterized by intermediate low Mg content and high Al values. Conversely, SU11 shows higher K values than the rest of the quadrangle, with a higher Mg content than SU6 and intermediate Al amount. SU9 in correspondence with Hokusai ejecta, shows intermediate to high Mg values and intermediate high to low Al amount. This confirms the spectral variability within Borealis Planitia-nsp, is linked with compositional changes. Furthermore, the presence of craters and surface features, may have influenced the original composition of the SUs identified in Borealis Planitia-nsp.

5.2. Spectral Units Corresponding to Localized Surface Features

In addition to the large scale SUs, we identified several localized spectral units associated with surface features. Below, we detail the characteristics of these SUs.

5.2.1. Nathair Facula and the Other Faculae

Nathair Facula, Mercury's highest-albedo surface feature (Besse et al., 2020; Prockter et al., 2010), belongs to SU7, and is characterized by very high R750 and very steep spectral slopes (see Figure 5 and Table 1). The central region of Nathair Facula (see region 1 (red) in Figure 8g) enclosing the vent, has R750 values $\sim 87\%$ higher than H05 average (Table 2; Figures 8a and 8b), and $\sim 46\%$ higher than the other faculae (R750 $\sim 0.082 \pm 0.019$).

Nathair Facula, which is 430 km north-east of Rachmaninoff basin, is one of the few faculae not inside an impact crater. The outer edge of the facula is gradational, but spectral measures reveal it occurs at a radial distance of about 140 km from its mid-point (Besse et al., 2020; Rothery et al., 2021). Slightly south of the facula center is located a steep-sided rimless pit, of irregular shape ~ 40 km wide and 3 km deep (Besse et al., 2020; Rothery et al., 2021). The facula is asymmetrical and includes a "compound vent." Rothery et al. (2021) suggest it has

Table 2
Average Values of the Spectral Parameters Calculated for the SUs Shown in Figure 5

Spectral Parameter Values for the Spectral Units								
SU	$S_{430-560}$	%H05	$S_{750-1000}$	%H05	$S_{430-1000}$	%H05	R750	%H05
SU1	2.571 ± 0.117	-4.1	0.503 ± 0.165	-45.7	1.458 ± 0.161	-24.7	0.139 ± 0.017	75.9
SU2	2.443 ± 0.164	-8.9	0.555 ± 0.112	-40.1	1.468 ± 0.136	-24.2	0.106 ± 0.007	34.2
SU3	2.411 ± 0.159	-10.1	0.633 ± 0.106	-31.7	1.595 ± 0.163	-17.6	0.095 ± 0.007	20.3
SU4	1.903 ± 0.352	-29.0	0.673 ± 0.136	-27.4	1.425 ± 0.179	-26.4	0.057 ± 0.006	-27.8
SU5	2.694 ± 0.106	0.4	1.037 ± 0.078	11.9	2.084 ± 0.114	7.6	0.067 ± 0.006	-15.2
SU6	3.054 ± 0.232	13.9	1.001 ± 0.093	8.0	2.179 ± 0.154	12.6	0.082 ± 0.007	3.8
SU7	3.197 ± 0.242	19.2	0.932 ± 0.078	0.5	2.155 ± 0.116	11.3	0.109 ± 0.015	38.0
SU8	2.499 ± 0.164	-6.8	0.833 ± 0.081	-10.1	1.723 ± 0.115	-11.0	0.072 ± 0.005	-8.9
SU9	2.630 ± 0.141	-1.9	0.815 ± 0.086	-12.1	1.750 ± 0.122	-9.6	0.086 ± 0.008	8.9
SU10	2.545 ± 0.154	-5.1	0.890 ± 0.071	-4.0	1.808 ± 0.117	-6.6	0.061 ± 0.003	-22.8
SU11	3.244 ± 0.412	21.0	1.275 ± 0.257	37.5	2.482 ± 0.294	28.2	0.065 ± 0.009	-17.7
H05	2.682 ± 0.378		0.927 ± 0.195		1.936 ± 0.286		0.079 ± 0.014	

Note. Columns indicated with %H05 report how SUs spectral parameters mean values exceed or are lower than H05 average.

been interested by different eruptive episodes, producing a migration of the locus of eruption. The morphological analysis of Nathair Facula indicates this area has been characterized by the most energetic and/or recent eruptions in the north eastern part of the vent, including slightly non-vertical eruption fountains (Rothery et al., 2021).

Nathair Facula superposes other geological units, in particular icp, where the central vent is located, and Borealis Planitia-nsp (Figure 8e), indicating the young age of this feature. Nathair Facula overlies the old icp (pre-Tolstojan-early Calorian age), but also the ejecta of the c4 Rachmaninoff basin (Kinczyk et al., 2020; Wright et al., 2019), suggesting the Facula is Mansurian or younger in age, which is almost certainly younger than 1.7 Ga and possibly younger than 0.85 Ga (Banks et al., 2017).

The RGB false-color composite image of Nathair Facula at 217 m/px in Figure 8a displays evident fresh bright mass wasted material spectrally bluer than the rest of the facula. The Clementine style color composite image in Figure 8c, highlights a different asymmetry of the facula, not visible in the RGB false-color and in the reflectance maps (Figures 8a and 8b), and it is probably conveying information about the underlying material (which is possible because facula material never constitutes the whole surface of any pixel). In Clementine style map (Figure 8c) the north eastern side on the map appears in orange color, indicating a spectral reddening with respect to the south western part, where the blue channel dominates. The RGB slopes map in Figure 8d confirms the trend of Figure 8c. $S_{430-1000}$ and $S_{430-560}$ slopes are steeper than the northern part of the halo (Figure 8d), whereas in the western side of the facula, $S_{750-1000}$ has higher values. Nathair Facula's average spectrum is one of the reddest of the entire quadrangle. The central region of Nathair Facula (Figure 8g, region 1 (red)) has $S_{430-560}$ and $S_{430-1000}$ average values ~15%–18% higher than the average of H05 (see Table 2). Furthermore, while $S_{430-1000}$ differs by only a few % from those of other faculae, the average $S_{430-560}$ value of Nathair Facula is ~10% steeper. This peculiar spectral behavior could be related with Nathair Facula composition, characterized by highest Ca/S ratio (probably indicating depletion in S) on the entire planet (Nittler et al., 2020; Weider et al., 2015; Figure 7). The asymmetric color of the halo in Figures 8c and 8d, could be linked to compositional variations caused by different mixing degrees of Nathair Facula material with background icp and Borealis Planitia-nsp.

A bright ray belonging to Fonteyn crater (see Section 5.2.3) superposes the facula. This ray has a similar, but lighter color with respect to the vent wall material in the Clementine style map (Figure 8c), indicating in both cases the presence of fresh material, with different mixing degree and/or composition.

Nathair Facula is the main feature included in SU7, but small areas within the most intense central parts of other faculae, for example, Suge Facula and Neidr Facula, also belong to SU7. In general, faculae show lower values of

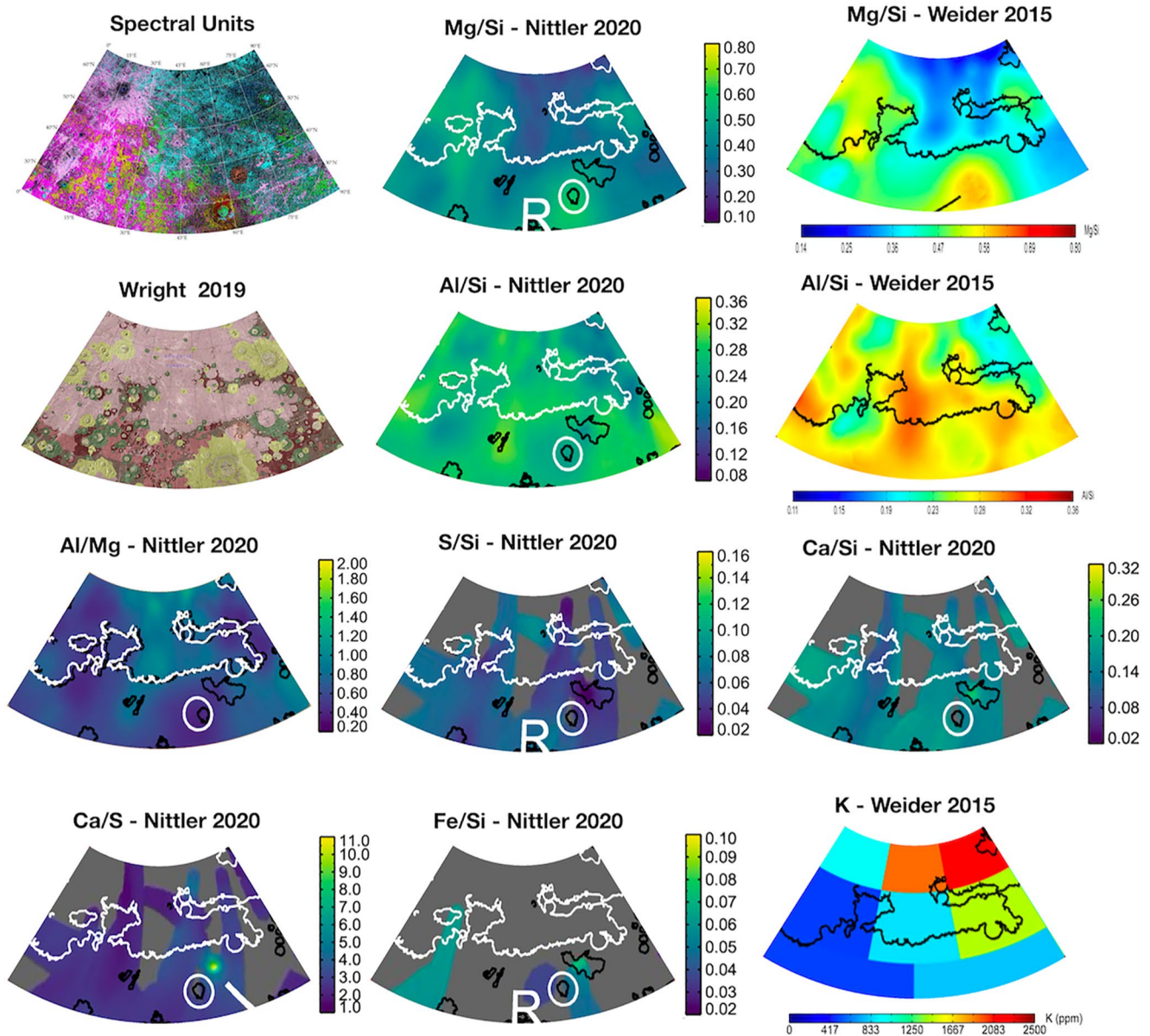


Figure 7. Comparison among spectral units defined in this work, morphostratigraphic map produced by Wright et al. (2019) and compositional maps published by Weider et al. (2015) and Nittler et al. (2020). The XRS and GRS maps shown in this figure, have been resized and adapted from the original ones to fit Hokusai quadrangle. Maps color scale and boundaries of Borealis Planitia northern smooth plains and other features follow those of the original figures.

all parameters than Nathair Facula, probably because they were emplaced as thinner deposits, and are included in the units SU6 and SU11, suggesting a composition similar to Borealis Planitia-nsp.

H05 contains ten other faculae most of which are interpreted as explosive volcanic deposits (Goudge et al., 2014; Kerber et al., 2011; Klimczak et al., 2018; Thomas et al., 2014b). We observed that faculae are mainly distributed in the southern part of the quadrangle, and overlying icp and ip units, or are located in the Borealis Planitia-nsp boundaries and are often linked with impact craters (Klimczak et al., 2018). Most faculae are associated with evident vents, with the notable exception of Suge Facula, within Rachmaninoff basin annulus, which is “pitted ground” (Thomas et al., 2014b).

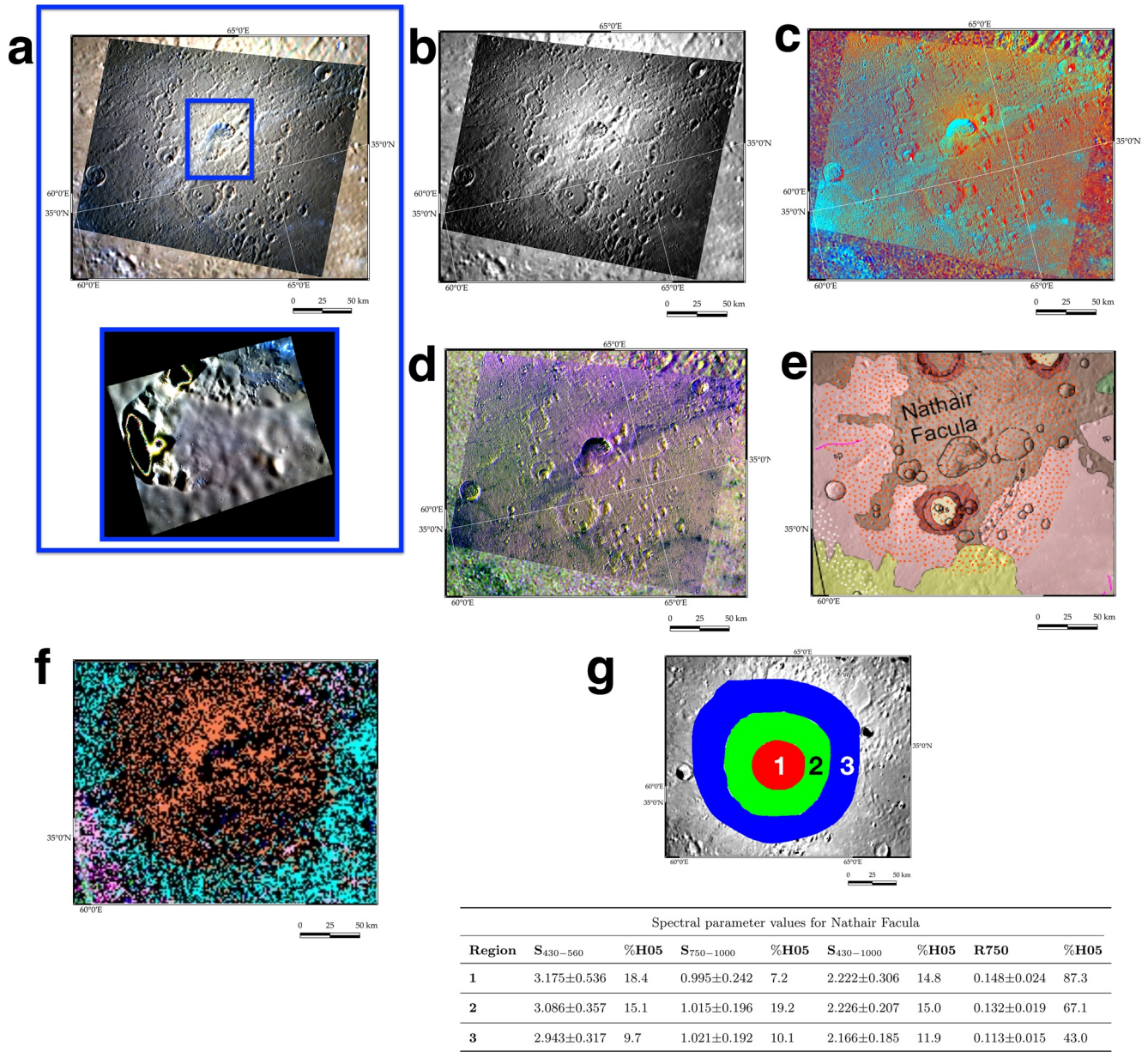


Figure 8. Nathair Facula at 217 m/px. (a) (top) Nathair Facula RGB “false color” mosaic: R: 1000 nm, G: 750 nm, B: 430 nm. In the bottom panel a close up of Nathair Facula vent is shown. (b) Nathair Facula reflectance map at 750 nm. (c) RGB “Clementine-like” color composite mosaic. (d) Nathair Facula RGB “spectral slopes” color composite mosaic”: R: $S_{430-1000}$, G: $S_{750-1000}$, B: $S_{430-560}$. (e) Nathair Facula morphostratigraphic map, close up from Figure 3e. (f) Nathair Facula spectral units map, close up from Figure 5a. (g) Average values of $S_{430-560}$, $S_{750-1000}$, $S_{430-1000}$ and R750 for regions 1 (red), 2 (green), 3 (blue) displayed in the upper image. Columns indicated with %H05 report how spectral slopes and reflectance for regions 1 (red), 2 (green) and 3 (blue) exceed or are lower compared with H05 average.

Figures 9a–9c show an example of a region containing a facula with a central vent and not related to impact craters, superposed on ip unit and surrounded by several craters with intermediate and high degradation degree (c1, c2), and a cluster of faculae associated with a crater rim in the northern side of the vent (Figure 9f).

Faculae stand out from the background in the RGB enhanced, Clementine-like and spectral slopes maps (Figures 9b–9d) and the most prominent is indicated with an orange stipple in the morphostratigraphic map (Figure 9f). Figure 9d highlights the spectral behavior of the faculae, which are distinguished from other terrains by the high $S_{430-560}$ values and by an increasing reflectance.

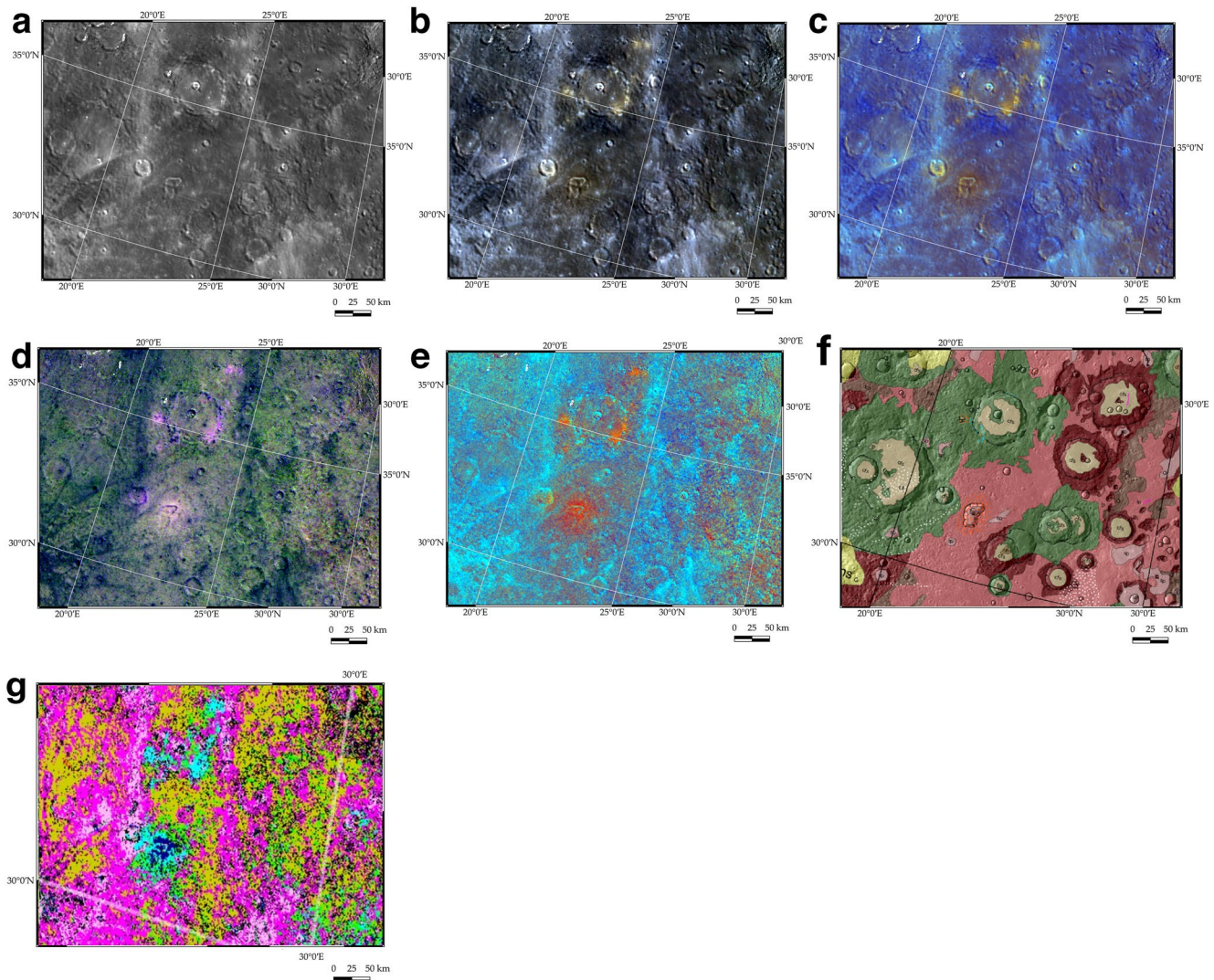


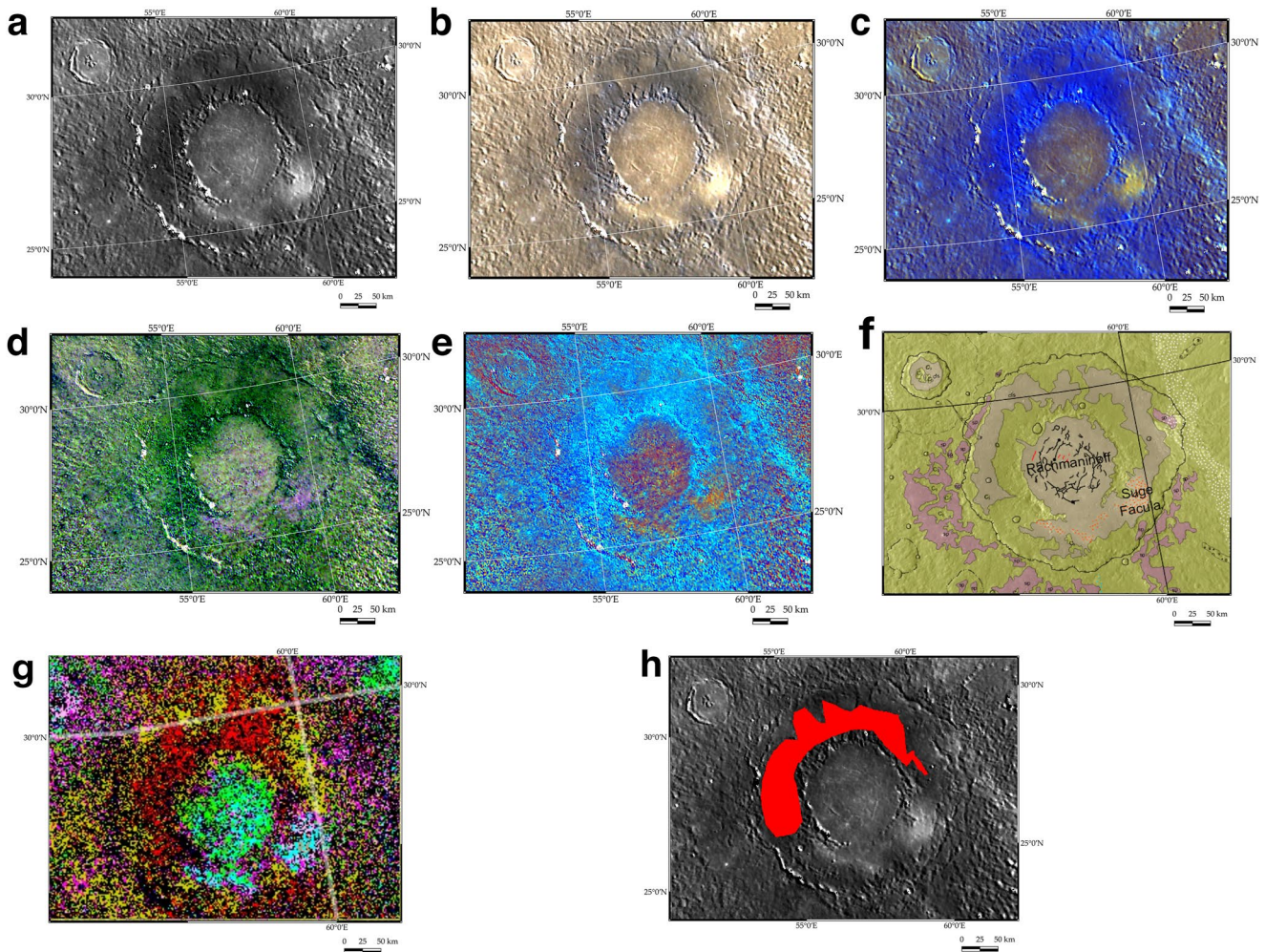
Figure 9. Close up of a group of faculae located in the south-western side of H05 quadrangle. The bottom facula shows a clear vent in the center. (a) R750 image of the selected region. (b) RGB “false color” mosaic: R: 1000 nm, G: 750 nm, B: 430 nm. (c) RGB “enhanced color” mosaic, R: PC2, G: PC1, B: 430/1000 nm. (d) RGB “spectral slopes” color composite mosaic: R: $S_{430-1000}$, G: $S_{750-1000}$, B: $S_{430-560}$. (e) RGB “Clementine-like” color composite mosaic, R: R (750 nm)/R (430 nm), G: R (750 nm)/R (1000 nm), and B: R (430 nm)/R (750 nm). (f) Morphostratigraphic map, close up of the region from Figure 3e. (g) Spectral units map for the selected area, close up from Figure 5a.

5.2.2. Rachmaninoff Basin and Its Low Reflectance Materials

The peak-ring Rachmaninoff basin ($D = \sim 290$ km; Figure 10a), located in south-eastern H05, is notable for containing the lowest surface elevation on Mercury, with a center ~ 5.8 km below the mean planetary radius (Figure 2e; Zuber et al., 2012). Prockter et al. (2010) dated the interior plains to be ~ 1 Ga. Rachmaninoff materials are classified as fresh crater material (c3) and smooth crater floor (cfs) by Wright et al. (2019) (Figure 10f), whereas on the Kinczyk et al. (2020) 5-class system, Wright et al. (2019) classified Rachmaninoff basin as a c4 crater.

Rachmaninoff basin-LRM belong to SU4 (red). This unit is characterized by very low reflectance, $S_{430-560}$ and $S_{430-1000}$, and shallow $S_{750-1000}$ (Figures 5, 10d, and 10e), and is restricted to just this area. Rachmaninoff basin is surrounded by SU8 and SU10, the SUs including icp and ip, while the floor inside the peak-ring hosts the intermediate unit SU5 and SU6 (Figure 10g). SU6 also extends to Suge Facula, which shows a very localized area belonging to SU7, the same unit found in Nathair Facula (see Section 5.2.1).

The annulus between the 130 km peak-ring and the basin rim contains a high concentration of LRM, as suggested by the low reflectance level (Figure 10a, 10b, and 10h). Suge Facula, located in south-eastern Rachmaninoff, is



Spectral parameter values for Rachmaninoff-LRM							
$S_{430-560}$	%H05	$S_{750-1000}$	%H05	$S_{430-1000}$	%H05	R750	%H05
2.135 ± 0.370	-20.4	0.872 ± 0.152	-5.9	1.553 ± 0.175	-19.8	0.052 ± 0.005	-34.2

Figure 10. Close up of Rachmaninoff basin located in the southern part of Hokusai quadrangle. (a) Reflectance map at 750 nm of Rachamaninoff basin. (b) RGB “false color” mosaic: R: 1000 nm, G: 750 nm, B: 430 nm. (c) RGB “enhanced color” mosaic, R: PC2, G: PC1, B: 430/1000 nm. (d) Rachamaninoff basin RGB “spectral slopes” color composite mosaic”: R: $S_{430-1000}$, G: $S_{750-1000}$, B: $S_{430-560}$. (e) Rachamaninoff basin RGB “Clementine-like” color composite mosaic: R: R (750 nm)/R (430 nm), G: R (750 nm)/R (1000 nm), and B: R (430 nm)/R (750 nm). (f) Morphostratigraphic map of Rachmaninoff basin, close up of the basin from Figure 3c. (g) Spectral units map of Rachmaninoff basin, close up from Figure 5a. (h) Average values of $S_{430-560}$, $S_{750-1000}$, $S_{430-1000}$ and R750 compared with H05 for the Rachmaninoff basin-LRM enclosed in the red area. Columns indicated with %H05 report how spectral slopes and reflectance for the red region are lower than H05 average.

a pitted ground, lacking any sign of vent (Thomas et al., 2014b). Rachmaninoff basin-LRM, concentrated in the annulus, is the lowest reflectance material in H05 (R750 is ~34% lower than the average of H05 (Figures 10h and Table 2), while peak-ring interior has reflectance similar to the terrains outside the crater (see Figure 10a). Rachmaninoff basin-LRM $S_{430-560}$ and $S_{430-1000}$ are ~20% shallower than the H05 average (see Figure 10h).

It stands out with darker/blue color in RGB enhanced mosaics, while the bright fresh craters and ray materials superimposed over older terrains display a light blue/cyan color (Figures 3b and 10c; Wright et al., 2019). RGB Clementine-like (Figures 3c and 10e) and spectral slopes mosaics (Figures 3d and 10d), which highlight only

spectral slope variations, indicate that Rachmaninoff basin-LRM has spectral slope behavior similar to bright rays and ejecta.

XRS data confirm that the spectral characteristics of this region are related to composition rather than other effects, recording high Mg and low Al content (Nittler et al., 2020; Weider et al., 2015; see Figure 7).

5.2.3. Bright Rays and Crater Ejecta Materials

Parts of H05 are overlain by both regionally extensive and localized ray systems, and related bright crater ejecta and crater walls. The maps shown in Figures 2a and 3a, highlight a clear reflectance contrast between the bright ejecta material and the surrounding regions. The bright fresh crater rays and ejecta, belonging to SU9, have R750 values up to ~9% higher, and shallower $S_{430-1000}$ and $S_{750-1000}$, with values ~9.6% and 12% lower, respectively, compared to the H05 average (Table 2). The spectral characteristics of the bright rays and ejecta can be more or less accentuated according to the age and mixing degree with the background terrains, but also could depend on the physical properties, for example, grain size as well as compositional variations, and a minor space weathering influence. The large spectral variability of the bright material is summarized in four SUs. In Figures 11 and 12, we show two representative examples of bright craters in the H05 quadrangle.

SU1 is characterized by very high R750 (~76% higher than H05 average) and very shallow $S_{430-1000}$ and $S_{750-1000}$ (~25% and ~46% lower than H05 average, respectively (Table 2)). This unit is localized in the walls of the craters and represents the freshest material of H05. We found this unit in the wall of Hodgkins crater (Figure 11). Hodgkins is a small rayed crater, located in the southern part of H05, and overlays the ejecta of a very degraded c1 crater (Figure 11f). In Figures 11a and 11b, Hodgkins rays are brighter than the underlying c1 and c2 craters. In particular, the Hodgkins crater walls appear very bright, and this contrast is clearly visible in the enhanced and Clementine map, where rays stand out in cyan color and in the spectral slopes maps, emphasizing the low $S_{430-1000}$ values. SU1, in Figure 11g, is enclosed by SU2, and we identified it as intermediate bright material, characterized by high R750 and shallow spectral slopes. The rays far from the crater, belong to SU9, which includes also Hokusai and Fonteyn rays, and SU3, showing spectral slopes shallower than H05 average but steeper than SU1 and SU2.

Figure 12 shows a c3 crater whose ejecta overlies the Borealis Planitia-nsp and icp units (Wright et al., 2019). There are no preserved rays at this crater, but it is surrounded by morphologically fresh continuous ejecta. In both the cases the ejecta are bluer than their surroundings, as expected for fresh material. This crater superimposes Borealis Planitia-nsp, as shown in the enhanced map in Figure 12c. The spectral slope map in Figure 12d, picks out with great accuracy the crater ejecta, as does the Clementine-like map in Figure 12e. This fresh crater overlaps the SU6 background unit, and includes SU1, SU2 and SU9 in the ejecta furthest from the rim (Figure 12g).

6. Summary and Conclusions

In this work, we analyze the spectral characteristics of the H05-Hokusai quadrangle on Mercury. We defined suitable spectral units starting from selected parameters, taking into account the main properties of the surface of Mercury. This approach allows us to study the spectral behavior of H05 quadrangle, but at the same time, to investigate the relationship with the morphology.

We identified 11 spectral units across H05 by thresholding the distribution values of four selected spectral parameters: reflectance at 750 nm and three significant spectral slopes: 430–1000 nm ($S_{430-1000}$), 430–560 nm ($S_{430-560}$) and 750–1000 nm ($S_{750-1000}$). Units SU5, SU6, SU8, SU9, SU10 and SU11 are identified at large-scale, whereas units SU1, SU2, SU3, SU4 and SU7 are picked out only in very localized regions and are associated mainly with superficial units, for example, Rachmaninoff basin - low reflectance material, bright rays and ejecta, and faculae.

Below we summarize the properties of the spectral units identified.

1. Large scale SUs
 - i. SU5 is characterized by intermediate values of the spectral parameters. We observe this unit in the transition region between the eastern and western side of Borealis Planitia northern smooth plains, in the floor

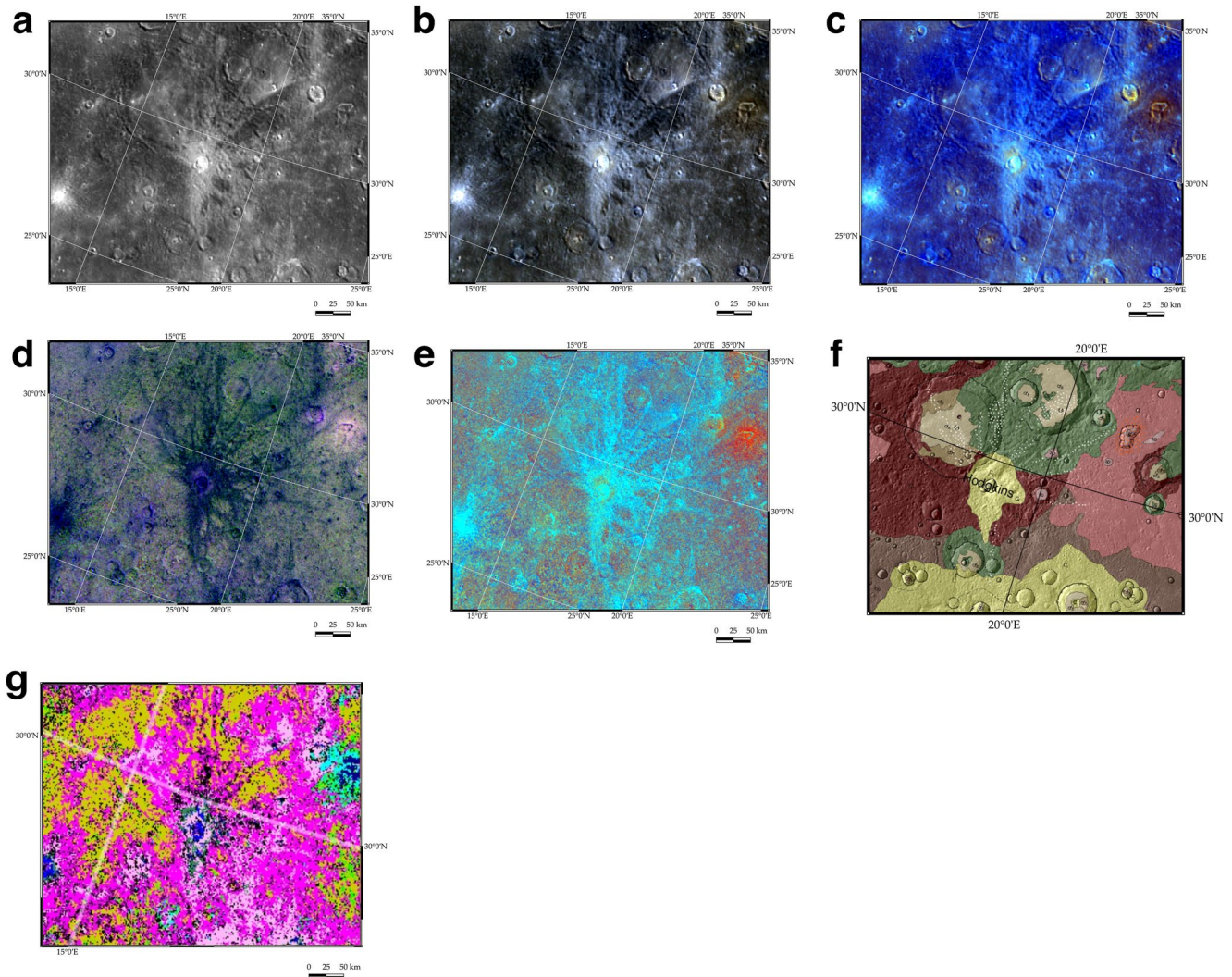


Figure 11. Small bright rayed crater in the southern side of Hokusai quadrangle, named Hodgkins. (a) Reflectance map at 750 nm of Hodgkins crater. (b) Hodgkins crater RGB “false color” mosaic: R: 1000 nm, G: 750 nm, B: 430 nm. (c) Hodgkins crater RGB “enhanced color” mosaic, R: PC2, G: PC1, B: 430/1000 nm (d) Hodgkins crater RGB “spectral slopes” color composite mosaic: R: $S_{430-1000}$, G: $S_{750-1000}$, B: $S_{430-560}$. (e) Hodgkins crater RGB “Clementine-like” color composite mosaic: R: $R(750\text{ nm})/R(430\text{ nm})$, G: $R(750\text{ nm})/R(1000\text{ nm})$, and B: $R(430\text{ nm})/R(750\text{ nm})$. (f) Hodgkins crater morphostratigraphic map, close up of the crater from Figure 3c. (g) Spectral units map of Hodgkins crater, close up from Figure 5a.

of Rachmaninoff basin and in the south-eastern part of the quadrangle, where the oldest morphostratigraphic units (intermediate plains and intercrater plains) are present.

- ii. SU6, characterized by high R_{750} values and spectral slopes, includes both the central area of Borealis Planitia-northern smooth plains, and parts of the faculae observed in H05, excluding Nathair which belongs to a separate unit (SU7).
- iii. The western side of Borealis Planitia-northern smooth plains is covered by SU8 and SU9. SU8 has intermediate-low reflectance at 750 nm, shallow spectral slopes, and includes intermediate plains, intercrater plains and part of the western side of Borealis Planitia. SU9, covering Hokusai and the main rays system of H05, shows intermediate–high reflectance at 750 nm and intermediate low $S_{430-560}$ and $S_{750-1000}$. Even though these units occur within Borealis Planitia-northern smooth plains, their spectral behavior is influenced by Hokusai rays and ejecta, intercrater plains and intermediate plains.
- iv. SU10 shows very low reflectance and shallow spectral slope. This unit is not linked with any particular morphostratigraphic unit, and is located mainly in the western part of H05, and in correspondence with Rachmaninoff basin rim and ejecta.

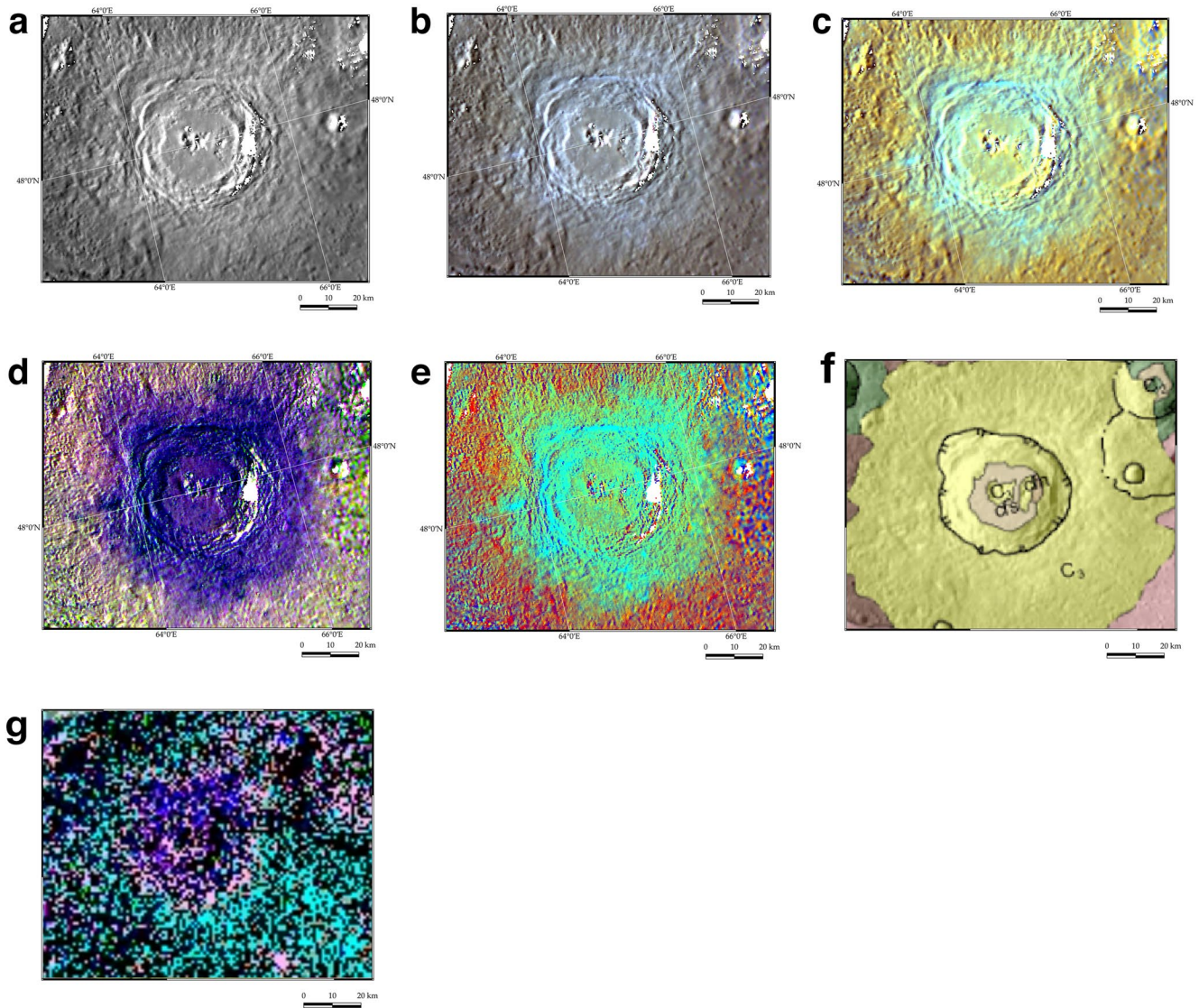


Figure 12. Small bright crater located in the center of Hokusai quadrangle. (a) Reflectance map at 750 nm of the crater. (b) RGB “false color” mosaic: R: 1000 nm, G: 750 nm, B: 430 nm. (c) RGB “enhanced color” mosaic: R: PC2, G: PC1, B: 430/1000 nm (d) RGB “spectral slope” color composite mosaic”: R: $S_{430-1000}$, G: $S_{750-1000}$, B: $S_{430-560}$. (e) RGB “Clementine-like” color composite mosaic: R: $R(750\text{ nm})/R(430\text{ nm})$, G: $R(750\text{ nm})/R(1000\text{ nm})$, and B: $R(430\text{ nm})/R(750\text{ nm})$. (f) Mophostratigraphic map, close up of the crater from Figure 3c. (g) Spectral units map of the crater, close up from Figure 5a.

- v. SU11 includes the eastern part of Borealis Planitia-northern smooth plains in correspondence of Rustaveli crater, and conversely to SU6, it has lower reflectance values but steep spectral slopes.

2. Local scale SUs

- i. SU7 is the unit corresponding to Nathair Facula and very localized areas within a few other faculae, for example, Suge and Neidr Facula. This unit shows very high R_{750} values and very steep $S_{430-560}$ and steep $S_{430-1000}$.
- ii. SU4 includes Rachmaninoff basin-low reflectance material. It shows very low reflectance at 750 nm, very shallow spectral slopes. It is the darker units of H05, indicating a high abundance of opaque mineralogical phases and impact melt.
- iii. We found localized SUs with higher reflectance than the H05 average and shallow spectral slopes (SU1, SU2, SU3). These units correspond to localized bright crater rays and ejecta of small craters distributed across the quadrangle. SU1 includes very fresh material, with very high reflectance at 750 nm and very shallow global slope and $S_{750-1000}$; SU2 shows intermediate bright crater materials, with high reflectance

at 750 nm and shallow spectral slopes; while SU3, which we named low bright materials, displays shallower spectral slopes than Hokusai average, but steeper than SU1 and SU2.

Spectral units analysis of H05-Hokusai quadrangle highlights spectral variations related to compositional diversity and/or terrain maturity.

The comparison between morphostratigraphic units identified by Wright et al. (2019) and spectral units, reveals that in some cases local SUs overlap the underlying morphostratigraphic unit, unlike large scale units. Sometimes, a single morphological unit includes more than one spectral unit. The most illustrative case is Borealis Planitia northern smooth plains, which covers the northern part of H05, and includes three large scale spectral units.

Large part of Borealis Planitia northern smooth plains in H05, is influenced by impacts. The western side is dominated by the widespread ejecta and rays of Hokusai crater. The presence of impact melt and the mixing between the superficial material and the underlying layers, modified the typical spectral behavior of the northern smooth plains, reducing both the reflectance and the spectral slopes.

The eastern part of Borealis Planitia is characterized by the large impact crater Rustaveli. In this case, no rays are present. From the spectral point of view there is a strong reflectance decreasing, maintaining high spectral slopes values. The impact may have been instrumental in determining the current spectral characteristics of this area. The exposure of opaque materials from the subsurface (Denevi et al., 2009; Ernst et al., 2010; Weider et al., 2015), mixed with the original Borealis Planitia terrains, could reduce the reflectance, keeping the steep spectral slopes we observe.

The central part of Borealis Planitia, not influenced by large impacts, shows high reflectance at 750 nm and steep spectral slopes, typical of the volcanic origin material. XRS data reveals elemental compositional variations within Borealis Planitia. The central part, corresponding with SU6, displays high Al/Mg ratio then the rest of the northern smooth plains in Hokusai quadrangle, confirming the composition of Borealis Planitia is strictly linked with the impacts history of this region. XRS maps show a higher Mg/Si ratio and lower Al/Si ratio on Mercury than the terrestrial and the lunar rocks, with low Fe and Ti concentration and an amount of S 10 times higher (Weider, 2018; Weider et al., 2015). Petrological studies suggest that Mercury's surface is dominated by Mg-rich mafic rocks, such as anorthositic norites or gabbros (Peplowski & Stockstill-Cahill, 2019). The area of Borealis Planitia in H05, has been classified by Weider et al. (2015) as intermediate-Mg northern plains. Lower Mg amount in the central part of Borealis planitia could indicate a mineralogy similar to trachyte or anorthositic gabbros (Peplowski & Stockstill-Cahill, 2019).

The southern region of H05 is instead characterized by the more ancient and densely cratered terrain of Mercury, the intercrater plains. We cannot associate a specific spectral unit at this morphology, which is characterized by low-intermediate low reflectance and intermediate or shallow spectral slopes.

Low reflectance material is common on Mercury (Denevi et al., 2009). In Hokusai quadrangle, the darker low reflectance material region is observed in Rachmaninoff basin annulus, the only area in H05 belonging to SU4. This basin, dated to the Mansurian age, appears darker and younger with shallower spectral slopes than intercrater and intermediate plains, suggesting composition plays a dominant role with respect to space weathering. Several studies (e.g., Klima et al., 2018; Murchie et al., 2015) indicate that the presence of C in the form of graphite, is the most suitable opaque phase for Mercury. Globally, the percentage of graphite is estimated ~ 1 wt%, while in low reflectance material it can reach ~ 5 wt% (Klima et al., 2018; Murchie et al., 2015). The low reflectance materials have been interpreted as a typical example of the exposure of Mercury graphite-rich floating crust, survived to impacts and volcanism. Rachmaninoff basin is also the region with the highest Mg/Si ratio other than Mercury's "high-Mg region." The spectral characteristics of this area and the high Mg level suggest that a Mg-rich magmatic body was excavated during the basin-forming event (Denevi et al., 2009).

The surface features, such as faculae and crater rays and ejecta, seem to have a better correspondence with the spectral units. Faculae belong to the same spectral unit observed in the central region of Borealis Planitia (SU6). Among all the faculae, Nathair emerges showing the most extreme spectral characteristics of the quadrangle, very high reflectance and very steep spectral slopes. This is one of the youngest feature present in H05, and the one with the most peculiar composition. Although Ca/S is quite homogeneous on Mercury, Nathair Facula is the only region showing the highest Ca/S ratio observed by XRS (Nittler et al., 2020; Weider et al., 2016). This suggests

the eruptions occurred in Nathair Facula, was characterized by exsolution of S- and C-bearing volatile species (Nittler et al., 2020; Weider et al., 2016).

Finally, crater rays and ejecta, the freshest material in H05, belong to several spectral units according to their mixing degree and maturity. Some very bright craters, show low $S_{750-1000}$ values. $S_{750-1000}$ is a very useful parameter to detect possible absorption around 1 μm , when negative values are observed (Thangjam et al., 2013). Some very bright ejecta and rays display the shallower $S_{750-1000}$ in the whole H05. Although we do not observe negative $S_{750-1000}$ in H05, and therefore, we cannot be confident about the presence of the 1 μm band, we cannot exclude these fresh unweathered features, could enclose higher amounts of brighter mineralogical phases with a very shallow 1 μm band (e.g., very low iron mafic silicates, and silicate glasses or plagioclase; Burns, 1993).

The study carried out so far on the H05-Hokusai quadrangle based on the spectral units analysis, leads the way for more comprehensive work, which can be extended to other quadrangles. Carli et al. (2020) apply a similar approach to the Kuiper quadrangle. This allows not only to focus on the local spectral properties of a region, but also to extend the analysis to the entire planet. Furthermore, the comparison between morphostratigraphic and spectral units allows to understand the relationship between spectral variations and morphology at local and potentially at global scale.

The definition of the spectral units has the advantage of simplifying the data interpretation, but also to ease the production of spectral maps in a semi-automatic and more objective way, and the integration with the morphostratigraphic units. The production of highly informative geological maps, in which both spectral and morphological information are simultaneously associated to a specific geomorphic unit, facilitate the interpretation of Mercury surface, adding details for the understanding of the geological evolution of the planet, not achievable by using separated morphostratigraphic or spectral/mineralogical maps.

This kind of work was already proposed by Semenzato et al. (2020), and better developed during the *No 776276-PLANMAP* project, ended in February 2021. This synergistic twofold approach is the key to improving our knowledge on the geological processes that affected Mercury's surface in relation to its composition. The integration between the spectral and morphostratigraphic units for the Hokusai quadrangle will be the subject of a subsequent work.

Appendix A: Spectral Parameter Thresholds

Here, we describe the SUs definition based on the spectral parameters shown in Sections 3.1 and 3.2.

In Table 1, we report the SUs identified for Hokusai quadrangle, with the relative indices values and their spectral characteristics. Below, we describe the steps of the method applied to define the SUs (Figures A1, A2, A3, A4, A5, and A6):

1. We considered the histograms of $R750$, $S_{430-560}$, $S_{750-1000}$ and $S_{430-1000}$ (Figure A1). We divided the range of values for each spectral parameter into a fixed number of intervals based on their histogram values distribution (Figure A1) and on their density scatter plots (Figure A2), then we chose the threshold intervals as described in Section 3.4 (see Figures A3, A4, A5, and A6).
2. We named the thresholds intervals, starting from the lower to the higher range of values, as follows (Figure A1a)
 - i. Very low values (VL)
 - ii. Low values (L)
 - iii. Intermediate low values (IL)
 - iv. Intermediate values (I)
 - v. Intermediate high values (IH)
 - vi. High values (H)
 - vii. Very high values (VH)
3. We assigned to each threshold interval a progressive number, $VL = 1$, $L = 2$, $IL = 3$, $I = 4$, $IH = 5$, $H = 6$, $VH = 7$, and we found all the possible combinations of these intervals for all the parameters.
4. The last step consists on the selection of the final spectral units. We selected all the most populated units and we merged together all the units with similar spectral characteristics, excluding those sparsely populated and less significant, while considering the final map resolution.

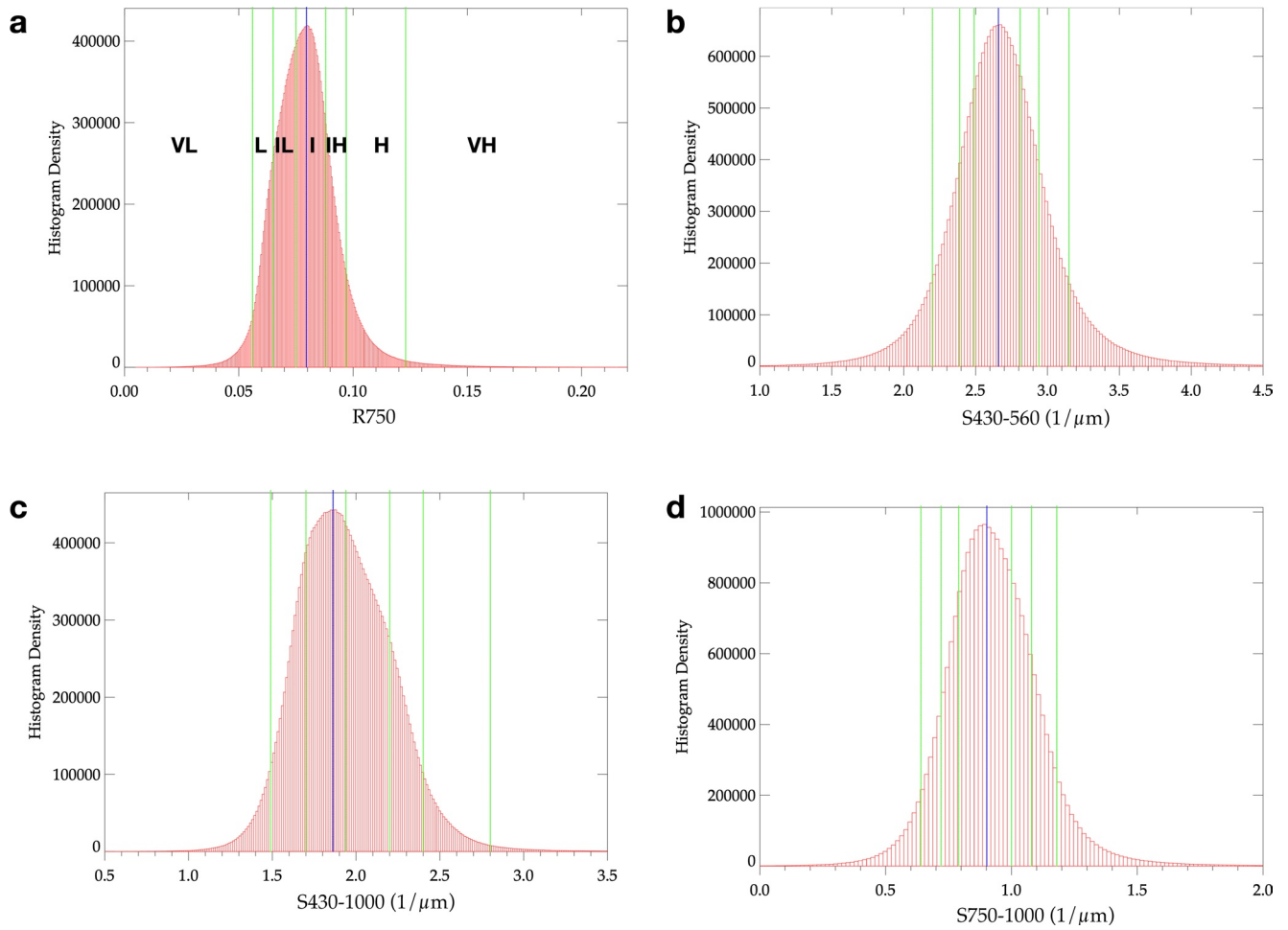


Figure A1. Hokusai histograms for (panel a) R_{750} , (panel b) $S_{430-560}$, (panel c) $S_{430-1000}$, (panel d) $S_{750-1000}$. Green lines indicate the threshold limits, while the blue line refers to the mode of the distribution.

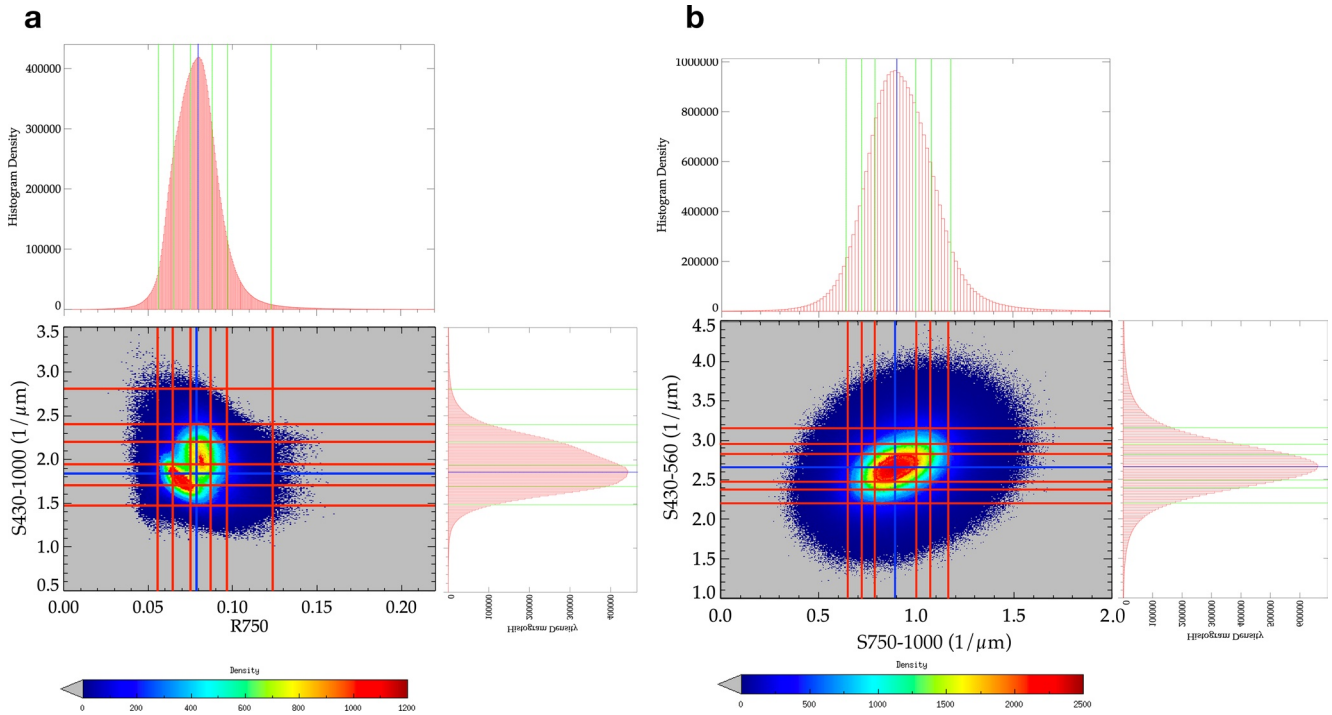


Figure A2. (a) $S_{430-1000}$ versus R_{750} density scatter plot and associated histograms as shown in Figure A1. (b) $S_{430-560}$ versus $S_{750-1000}$ density scatter plot with the corresponding histograms (Figure A1). Red lines indicate the interval thresholds, while the blue line indicates the mode value.

R750

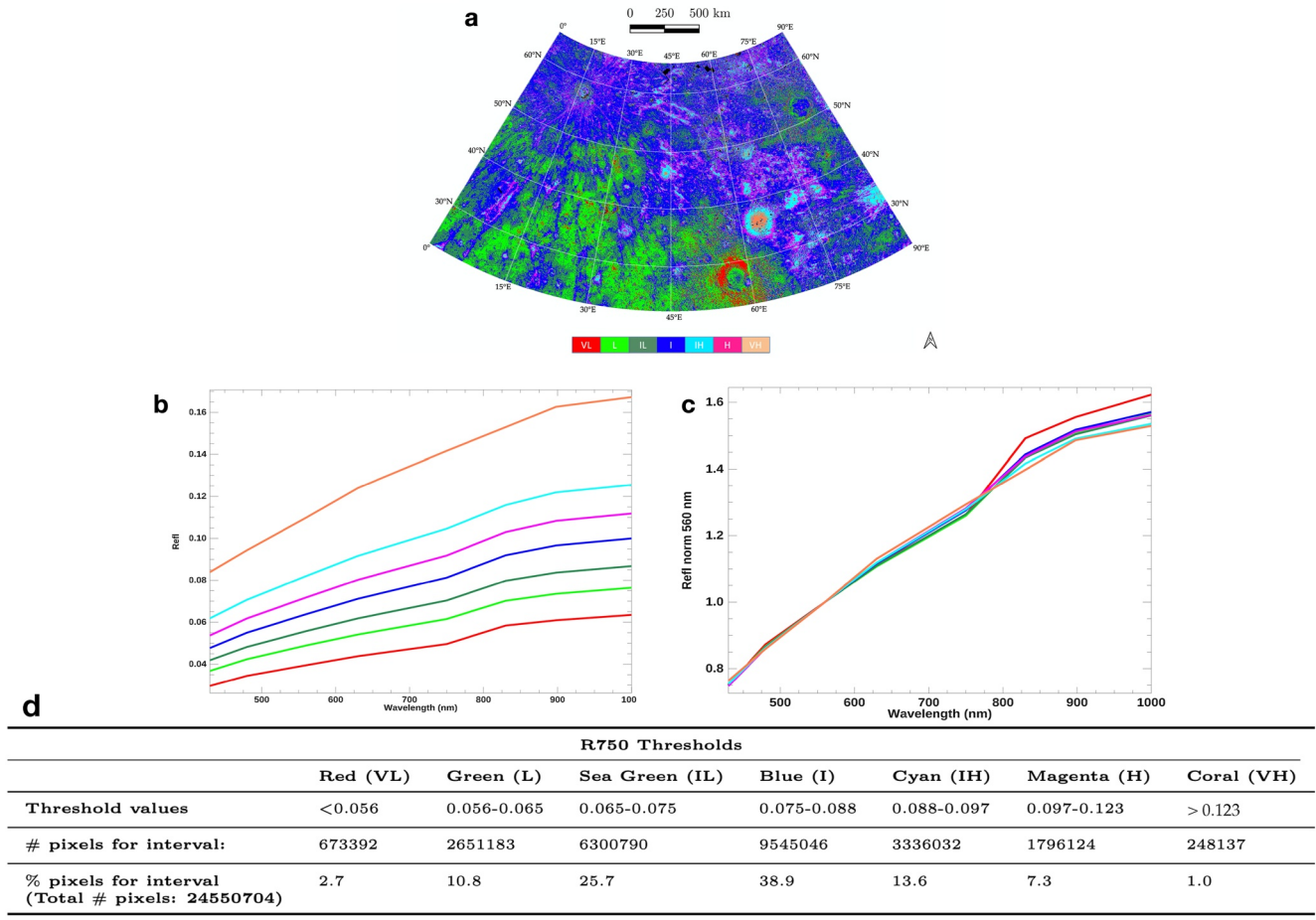


Figure A3. Map in panel (a) displays the thresholds classes obtained for R750. Each color refers to a specific class. Panel (b) shows the average reflectance spectra of the corresponding classes, while panel (c) exhibits the same spectra normalized at 560 nm. (d) Threshold values table for R750.

S430-1000

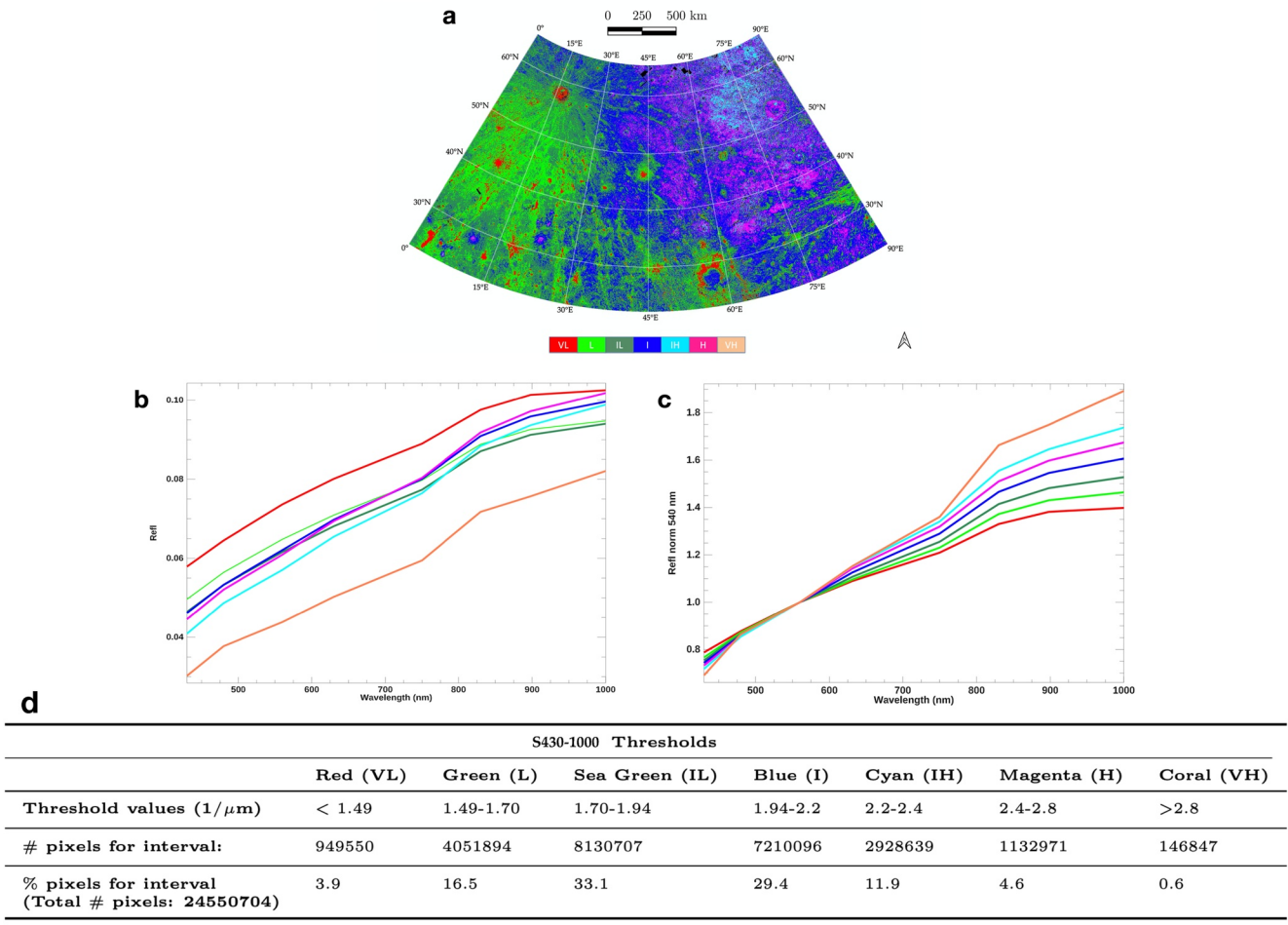


Figure A4. Map in panel (a) evinces the thresholds classes obtained for $S_{430-1000}$. Classes colors refer to the corresponding color spectra. Panel (b) shows the average reflectance spectra of the classes in panel (a), while panel (c) exhibits the same spectra normalized at 560 nm. (d) Threshold values table for $S_{430-1000}$.

S430-560

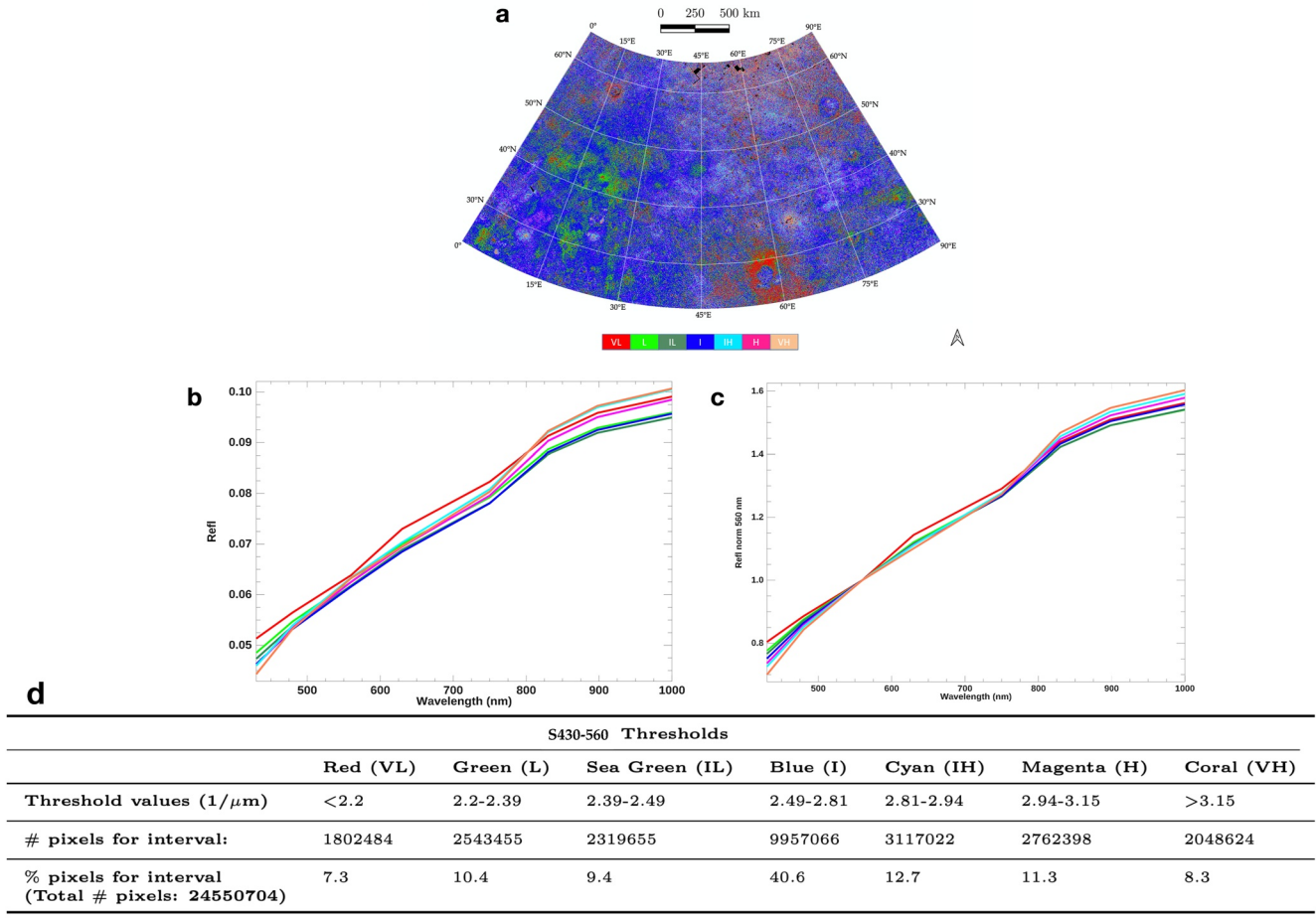


Figure A5. Panel (a) shows the threshold classes obtained for $S_{430-560}$. Panels (b and c) show the average reflectance spectra of the corresponding classes before and after the normalization at 560 nm respectively. (d) Threshold values table for $S_{430-560}$.

S750-1000

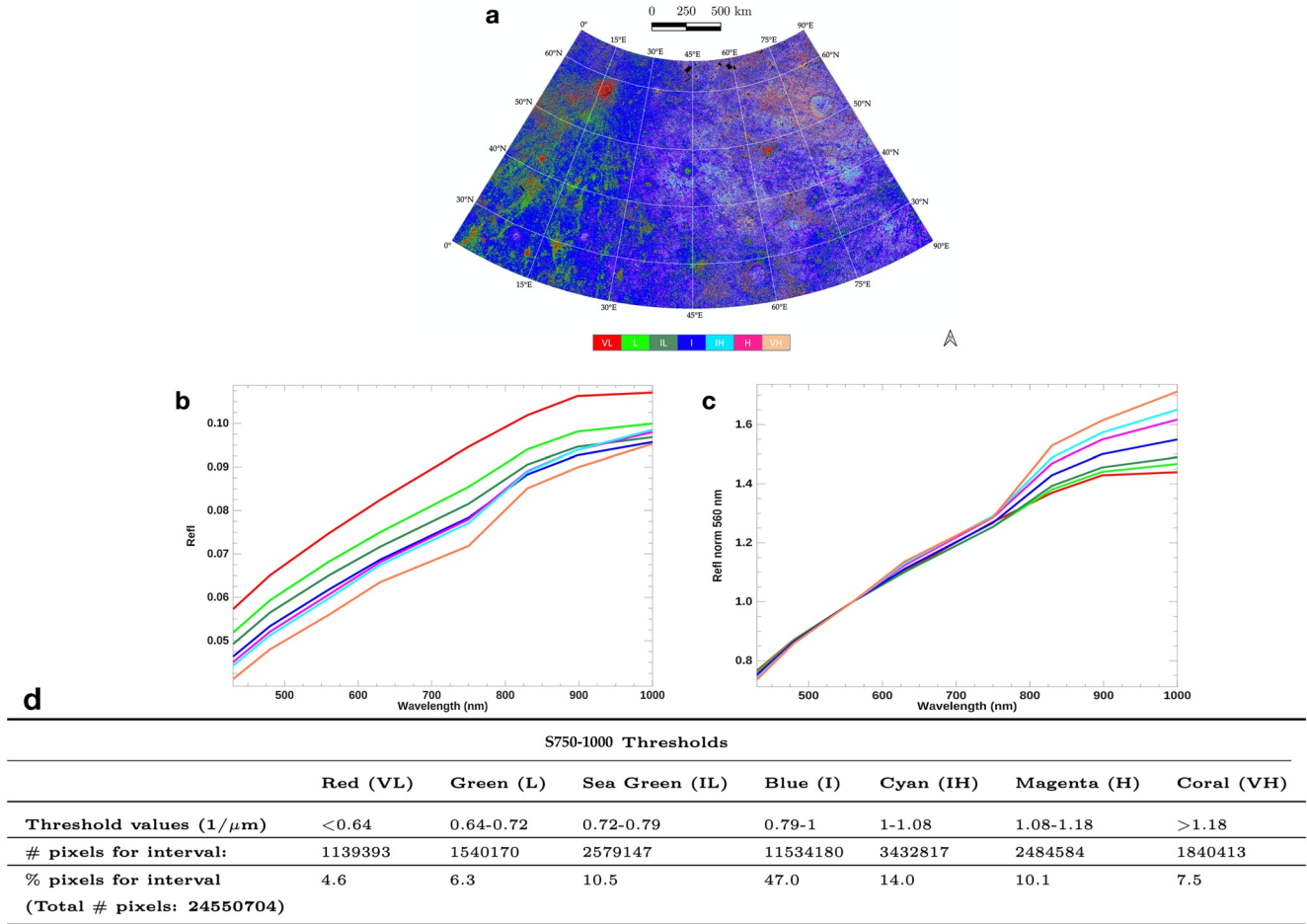


Figure A6. Map in panel (a) displays the threshold classes obtained for $S_{750-1000}$. As with Figures A3, A4, A5, each color refers to a specific class and the threshold values for each interval are reported in the table underneath (panel d). Panel (b) shows the average reflectance spectra of the corresponding classes, while panel (c) displays the same spectra normalized at 560 nm.

Data Availability Statement

This work is based on MESSENGER/MDIS-WAC data publicly available at <https://ode.rsl.wustl.edu/Mercury/indexproductsearch.aspx>. The high level products shown in this paper are available Zambon et al. (2019); Zambon et al. (2020).

References

Adams, J. B., & McCord, T. B. (1971). Optical properties of mineral separates, glass, and anorthositic fragments from Apollo mare samples. *Lunar and Planetary Science Conference Proceedings*, 2, 2183.

Banks, M. E., Xiao, Z., Braden, S. E., Barlow, N. G., Chapman, C. R., Fassett, C. I., & Marchi, S. S. (2017). Revised constraints on absolute age limits for Mercury’s Kuiperian and Mansurian stratigraphic systems. *Journal of Geophysical Research: Planets*, 122(5), 1010–1020. <https://doi.org/10.1002/2016JE005254>

Barnouin, O. S., Ernst, C. M., & Susorney, H. C. M. (2015). The remarkable Hokusai crater, Mercury. In *Lunar and planetary science conference* (p. 2672).

Besse, S., Doressoundiram, A., Barraud, O., Griton, L., Cornet, T., Muñoz, C., et al. (2020). Spectral properties and physical extent of pyroclastic deposits on Mercury: Variability within selected deposits and implications for explosive volcanism. *Journal of Geophysical Research*, 125(5), e05879. <https://doi.org/10.1029/2018JE005879>

Blewett, D. T., Chabot, N. L., Denevi, B. W., Ernst, C. M., Head, J. W., Izenberg, N. R., et al. (2011). Hollows on Mercury: MESSENGER evidence for geologically recent volatile-related activity. *Science*, 333, 1856–1859. <https://doi.org/10.1126/science.1211681>

Blewett, D. T., Hawke, B. R., Lucey, P. G., & Robinson, M. S. (2007). A mariner 10 color study of mercurian craters. *Journal of Geophysical Research*, 112, E02005. <https://doi.org/10.1029/2006JE002713>

Acknowledgments

This work is funded by the European Union’s Horizon 2020 research grant agreement No 776276-PLANMAP (<https://planmap.eu/>) and by the Italian Space Agency (ASI) within the SIMBIO-SYS project (ASI-INAF agreement 2017-47-H.0). Open Access Funding provided by Istituto nazionale di astrofisica within the CRUI-CARE Agreement.

- Blewett, D. T., Lucey, P. G., Hawke, B., Ling, G. G., & Robinson, M. S. (1997). A comparison of mercurian reflectance and spectral quantities with those of the Moon. *Icarus*, *129*(1), 217–231. <https://doi.org/10.1006/icar.1997.5785>
- Blewett, D. T., Robinson, M. S., Denevi, B. W., Gillis-Davis, J. J., Head, J. W., Solomon, S. C., et al. (2009). Multispectral images of Mercury from the first MESSENGER flyby: Analysis of global and regional color trends. *Earth and Planetary Science Letters*, *285*, 272–282. <https://doi.org/10.1016/j.epsl.2009.02.021>
- Blewett, D. T., Stadermann, A. C., Susorney, H. C., Ernst, C. M., Xiao, Z., Chabot, N. L., et al. (2016). Analysis of MESSENGER high-resolution images of Mercury's hollows and implications for hollow formation. *Journal of Geophysical Research: Planets*, *121*, 1798–1813. <https://doi.org/10.1002/2016JE005070>
- Blewett, D. T., Vaughan, W. M., Xiao, Z., Chabot, N. L., Denevi, B. W., Ernst, C. M., et al. (2013). Mercury's hollows: Constraints on formation and composition from analysis of geological setting and spectral reflectance. *Journal of Geophysical Research: Planets*, *118*, 1013–1032. <https://doi.org/10.1029/2012JE004174>
- Bott, N., Doressoundiram, A., Zambon, F., Carli, C., Guzzetta, L., Perna, D., & Capaccioni, F. (2019). Global spectral properties and lithology of Mercury: The example of the Shakespeare (H-03) quadrangle. *Journal of Geophysical Research: Planets*, *124*(9), 2326–2346. <https://doi.org/10.1029/2019JE005932>
- Burns, R. (1993). *Mineralogical applications of crystal field theory* (2nd ed.). Cambridge University Press.
- Carli, C., Giacomini, L., Zambon, F., Ferrari, S., Massironi, M., Galluzzi, V., & Palumbo, P. (2020). Kuiper quadrangle spectral analysis: Looking forward to integrated geological map. In *European planetary science congress* (pp. EPSC2020–367).
- Clark, R. N. (1999). *Remote sensing for the Earth sciences - Manual of remote sensing* (Vol. 3). John Wiley and Sons.
- Clark, R. N., Fanale, F. P., & Gaffey, M. J. (1986). Surface composition of natural satellites. In J. A. Burns, & M. S. Matthews (Eds.), *Surface composition of natural satellites* (pp. 437–491). <https://doi.org/10.2307/j.ctv1v3gr3r.14>
- Cloutis, E. A., Sunshine, J. M., & Morris, R. V. (2004). Spectral reflectance-compositional properties of spinels and chromites: Implications for planetary remote sensing and geothermometry. *Meteoritics & Planetary Sciences*, *39*(4), 545–565. <https://doi.org/10.1111/j.1945-5100.2004.tb00918.x>
- Cuzzi, J., Clark, R., Filacchione, G., French, R., Johnson, R., Marouf, E., & Spilker, L. (2009). Ring particle composition and size distribution. In M. K. Dougherty, L. W. Esposito, & S. M. Krimigis (Eds.), *Saturn from Cassini-Huygens* (pp. 459–509). https://doi.org/10.1007/978-1-4020-9217-6_15
- Davies, M. E. (1976). *A mariner 10 atlas of Mercury*. Reports of Accomplishments of Planetology Programs.
- Denevi, B. W., Chabot, N. L., Murchie, S. L., Becker, K. J., Blewett, D. T., Domingue, D. L., et al. (2018). Calibration, projection, and final image products of MESSENGER's Mercury dual imaging system. *Space Science Reviews*, *214*(1), 2. <https://doi.org/10.1007/s11214-017-0440-y>
- Denevi, B. W., Ernst, A., Meyer, H. M., Robinson, M. S., Murchie, S., Whitten, J. L., et al. (2013). The distribution and origin of smooth plains on Mercury. *Journal of Geophysical Research*, *118*, 891–907. <https://doi.org/10.1002/jgre.20075>
- Denevi, B. W., & Robinson, M. S. (2008). Mercury's albedo from Mariner 10: Implications for the presence of ferrous iron. *Icarus*, *197*, 239–246. <https://doi.org/10.1016/j.icarus.2008.04.021>
- Denevi, B. W., Robinson, M. S., Boyd, A. K., Sato, H., Hapke, B. W., & Hawke, B. R. (2014). Characterization of space weathering from lunar reconnaissance orbiter camera ultraviolet observations of the Moon. *Journal of Geophysical Research: Planets*, *119*(5), 976–997. <https://doi.org/10.1002/2013JE004527>
- Denevi, B. W., Robinson, M. S., Solomon, S. C., Murchie, S. L., Blewett, D. T., Domingue, D. L., et al. (2009). The evolution of Mercury's crust: A global perspective from MESSENGER. *Science*, *324*, 613–618. <https://doi.org/10.1126/science.1172226>
- Domingue, D. L., Denevi, B. W., Murchie, S. L., & Hash, C. D. (2016). Application of multiple photometric models to disk-resolved measurements of Mercury's surface: Insights into Mercury's regolith characteristics. *Icarus*, *268*, 172–203. <https://doi.org/10.1016/j.icarus.2015.11.040>
- Ernst, C. M., Denevi, B. W., & Ostrach, L. R. (2017). Updated absolute age estimates for the Tolstoj and Caloris Basins, Mercury. In *Lunar and planetary science conference* (p. 2934).
- Ernst, C. M., Murchie, S. L., Barnouin, O. S., Robinson, M. S., Denevi, B. W., Blewett, D. T., et al. (2010). Exposure of spectrally distinct material by impact craters on Mercury: Implications for global stratigraphy. *Icarus*, *209*, 210–223. <https://doi.org/10.1016/j.icarus.2010.05.022>
- Filacchione, G., Capaccioni, F., Ciarnello, M., Clark, R. N., Cuzzi, J. N., Nicholson, P. D., et al. (2012). Saturn's icy satellites and rings investigated by cassini-VIMS: III – radial compositional variability. *Icarus*, *320*, 1064–1096. <https://doi.org/10.1016/j.icarus.2012.06.040>
- Galluzzi, V., Ferranti, L., Massironi, G. M., Palumbo, P., Guzzetta, L., & Palumbo, P. (2019). Structural analysis of the victoria quadrangle fault systems on Mercury: Timing, geometries, kinematics, and relationship with the high-mg region. *Journal of Geophysical Research: Planets*, *124*(10), 2543–2562. <https://doi.org/10.1029/2019JE005953>
- Galluzzi, V., Guzzetta, L., Ferranti, L., Di Achille, G., Rothery, D. A., & Palumbo, P. (2016). Geology of the victoria quadrangle (h02), Mercury. *Journal of Maps*, *12*, 227–238. <https://doi.org/10.1080/17445647.2016.1193777>
- Galluzzi, V., Guzzetta, L., Mancinelli, P., Giacomini, L., Lewang, A. M., Malliband, C., & Palumbo, P. (2018). The making of the 1:3M Geological map series of Mercury: Status and updates. In *Mercury: Current and future science of the innermost planet* (Vol. 2047, p. 6075).
- Giacomini, L., Galluzzi, V., Carli, C., Massironi, M., Ferranti, L., & Palumbo, P. (2018). Updates on geologic mapping of Kuiper (H06) quadrangle. In *European planetary science congress* (pp. EPSC2018–721).
- Giberson, W. E., & Cunningham, N. W. (1975). Mariner 10 mission to Venus and Mercury. *Acta Astronautica*, *2*, 715–743. [https://doi.org/10.1016/0094-5765\(75\)90012-0](https://doi.org/10.1016/0094-5765(75)90012-0)
- Gouge, T. A., Head, J. W., Kerber, L., Blewett, D. T., Denevi, B. W., Domingue, D. L., et al. (2014). Global inventory and characterization of pyroclastic deposits on Mercury: New insights into pyroclastic activity from MESSENGER orbital data. *Journal of Geophysical Research: Planets*, *119*, 635–658. <https://doi.org/10.1002/2013JE004480>
- Guzzetta, L., Galluzzi, V., Ferranti, L., & Palumbo, P. (2017). Geology of the Shakespeare quadrangle (h03), Mercury. *Journal of Maps*, *13*(2), 227–238. <https://doi.org/10.1080/17445647.2017.1290556>
- Hawkins, S. E., Boldt, J. D., Darlington, E. H., Espiritu, R., Gold, R. E., Gotwols, B., et al. (2007). The Mercury dual imaging system on the MESSENGER spacecraft. *Space Science Reviews*, *131*(1–4), 247–338. <https://doi.org/10.1007/s11214-007-9266-3>
- Icarus special issue. (2014). The geology of vesta. *Icarus*, *244*.
- Icarus special issue. (2015). Vesta's surface composition. *Icarus*, *259*.
- Icarus special issue. (2018). The geologic mapping of ceres. *Icarus*, *316*.
- Icarus special issue. (2019). The composition of ceres. *Icarus*, *318*.
- Kerber, L., Head, J. W., Blewett, D. T., Solomon, S. C., Wilson, L., Murchie, S. L., et al. (2011). The global distribution of pyroclastic deposits on Mercury: The view from MESSENGER flybys 1-3. *Planetary and Space Science*, *59*, 1895–1909. <https://doi.org/10.1016/j.pss.2011.03.020>
- Kinczyk, M. J., Prockter, L. M., Byrne, P. K., Denevi, B. W., Buczkowski, D. L., Ostrach, L. R., & Miller, E. B. (2019). The first global geological map of mercury. In *EPSC-DPS Joint Meeting 2019* (Vol. 2019, pp. EPSC-DPS2019).

- Kinczyk, M. J., Prockter, L. M., Byrne, P. K., Susorney, H. C. M., & Chapman, C. R. (2020). A morphological evaluation of crater degradation on Mercury: Revisiting crater classification with MESSENGER data. *Icarus*, *341*, 113637. <https://doi.org/10.1016/j.icarus.2020.113637>
- Klima, R. L., Denevi, B. W., Ernst, C. M., Murchie, S. L., & Peplowski, P. N. (2018). Global distribution and spectral properties of low-reflectance material on Mercury. *Geophysical Research Letters*, *45*, 2945–2953. <https://doi.org/10.1002/2018gl077544>
- Klimczak, C., Crane, K. T., Habermann, M. A., & Byrne, P. K. (2018). The spatial distribution of Mercury's pyroclastic activity and the relation to lithospheric weaknesses. *Icarus*, *315*, 115–123. <https://doi.org/10.1016/j.icarus.2018.06.020>
- Lewang, A. M., Hiesinger, H., Bernhardt, H., Galluzzi, V., Guzzetta, L., & Massironi, M. (2018). Preliminary geologic map of the Beethoven basin, Mercury. In *Lunar and planetary science conference* (p. 1846).
- Lucchetti, A., Pajola, M., Galluzzi, V., Giacomini, L., Carli, C., Cremonese, G., et al. (2018). Mercury hollows as remnants of original bedrock materials and devolatilization processes: A spectral clustering and geomorphological analysis. *Journal of Geophysical Research: Planets*, *123*(9), 2365–2379. <https://doi.org/10.1029/2018JE005722>
- Lucey, P. G., Blewett, D. T., & Jolliff, B. L. (2000). Lunar iron and titanium abundance algorithms based on final processing of Clementine ultraviolet-visible images. *Journal of Geophysical Research*, *105*, 20297–20305. <https://doi.org/10.1029/1999JE001117>
- Lucey, P. G., & Riner, M. A. (2011). The optical effects of small iron particles that darken but do not redden: Evidence of intense space weathering on Mercury. *Icarus*, *212*(2), 451–462. <https://doi.org/10.1016/j.icarus.2011.01.022>
- Malliband, C. C., Rothery, D. A., Balme, M. R., & Conway, S. J. (2018). 1:3million scale geological mapping of the Derain quadrangle, Mercury. In *European planetary science congress* (pp. EPSC2018–908).
- Man, B., Rothery, D. A., Balme, M. R., Conway, S. J., & Wright, J. (2020). Geological mapping of the Neruda quadrangle (H13), Mercury. In *Egu general assembly conference abstracts* (p. 22131).
- Mancinelli, P., Minelli, F., Pauselli, C., & Federico, C. (2016). Geology of the raditladi quadrangle, Mercury (h04). *Journal of Maps*, *12*, 190–202. <https://doi.org/10.1080/17445647.2016.1191384>
- Murchie, S. L., Klima, R. L., Denevi, B. W., Ernst, C. M., Keller, M. R., Domingue, D. L., et al. (2015). Orbital multispectral mapping of Mercury with the MESSENGER Mercury dual imaging system: Evidence for the origins of plains units and low-reflectance material. *Icarus*, *254*, 287–305. <https://doi.org/10.1016/j.icarus.2015.03.027>
- Murray, B. C. (1975). The mariner 10 pictures of Mercury: An overview. *Journal of Geophysical Research*, *80*(B17), 2342–2344. <https://doi.org/10.1029/JB080i017p02342>
- Ngoc, N. B., Bott, N., & Diep, P. N. (2020). Spectral properties of the surface reflectance of the northern polar region of Mercury. *Research in Astronomy and Astrophysics*, *20*(3), 034. <https://doi.org/10.1088/1674-4527/20/3/34>
- Nittler, L. R., Frank, E. A., Weider, S. Z., Crapster-Pregont, E., Vorburget, A., Starr, R. D., & Solomon, S. C. (2020). Global major-element maps of Mercury from four years of MESSENGER X-ray spectrometer observations. *Icarus*, *345*, 113716. <https://doi.org/10.1016/j.icarus.2020.113716>
- Noble, S. K., & Pieters, C. M. (2003). Space weathering on Mercury: Implications for remote sensing. *Solar System Research*, *37*(1), 31–35. <https://doi.org/10.1023/a:1022395605024>
- Pegg, D. L., Rothery, D. A., Balme, M. R., & Conway, S. J. (2018). Geological mapping of the Debussy quadrangle (H-14) preliminary results. *Mercury: Current and future science of the innermost planet*, 2047, 6021.
- Peplowski, P. N., & Stockstill-Cahill, K. (2019). Analytical identification and characterization of the major geochemical terranes of Mercury's northern hemisphere. *Journal of Geophysical Research: Planets*, *124*(9), 2414–2429. <https://doi.org/10.1029/2019JE005997>
- Pieters, C. M., & Noble, S. K. (2016). Space weathering on airless bodies. *Journal of Geophysical Research: Planets*, *121*(10), 1865–1884. <https://doi.org/10.1002/2016JE005128>
- Pieters, C. M., Staid, M. I., Fischer, E. M., Tompkins, S., & He, G. (1994). A sharper view of impact craters from clementine data. *Science*, *266*, 1844–1848. <https://doi.org/10.1126/science.266.5192.1844>
- Pieters, C. M., Taylor, L. A., Noble, S. K., Keller, L. P., Hapke, B., Morris, R. V., et al. (2000). Space weathering on airless bodies: Resolving a mystery with lunar samples. *Meteoritics & Planetary Sciences*, *35*, 1101–1107. <https://doi.org/10.1111/j.1945-5100.2000.tb01496.x>
- Pieters, C. M., & Tompkins, S. (2005). Remote sensing of lunar mineralogy: The glass conundrum. In S. Mackwell, & E. Stansbery (Eds.), *36th annual lunar and planetary science conference* (p. 1346).
- Preusker, F., Stark, A., Oberst, J., Matz, K.-D., Gwinner, K., Roatsch, T., & Watters, T. R. (2017). Toward high-resolution global topography of Mercury from MESSENGER orbital stereo imaging: A prototype model for the H6 (kuiper) quadrangle. *Planetary and Space Science*, *142*, 26–37. <https://doi.org/10.1016/j.pss.2017.04.012>
- Prockter, L. M., Ernst, C. M., Denevi, B. W., Chapman, C. R., Head, J. W., Fassett, C. I., et al. (2010). Evidence for young volcanism on Mercury from the third MESSENGER flyby. *Science*, *329*(5992), 668–671. <https://doi.org/10.1126/science.1188186>
- Rava, B., & Hapke, B. (1987). An analysis of the Mariner 10 color ratio map of Mercury. *Icarus*, *71*(3), 397–429. [https://doi.org/10.1016/0019-1035\(87\)90037-6](https://doi.org/10.1016/0019-1035(87)90037-6)
- Riner, M. A., Lucey, P. G., Desch, S. J., & McCubbin, F. M. (2009). Nature of opaque components on Mercury: Insights into a mercurian magma ocean. *Geophysical Research Letters*, *36*(2), L02201. <https://doi.org/10.1029/2008GL036128>
- Robinson, M. S., Murchie, S. L., Blewett, D. T., Domingue, D. L., Hawkins, S. E., Head, J. W., et al. (2008). Reflectance and color variations on Mercury: Regolith processes and compositional heterogeneity. *Science*, *321*(5885), 66–69. <https://doi.org/10.1126/science.1160080>
- Rothery, D. A., Barraud, O., Besse, S., Carli, C., Pegg, D. L., Wright, J., & Zambon, F. (2021). On the asymmetry of Nathair facula. *Icarus*, *417*(107300), 114180. <https://doi.org/10.1016/j.icarus.2020.114180>
- Semenzato, A., Massironi, M., Ferrari, S., Galluzzi, V., Rothery, D. A., Pegg, D. L., et al. (2020). An integrated geologic map of the rembrandt basin, on Mercury, as a starting point for stratigraphic analysis. *Remote Sensing*, *12*(19), 3213. <https://doi.org/10.3390/rs12193213>
- Solomon, S. C., McNutt, R. L., Gold, R. E., & Domingue, D. L. (2007). MESSENGER mission overview. *Space Science Reviews*, *131*(1–4), 3–39. <https://doi.org/10.1007/s11214-007-9247-6>
- Solomon, S. C., Nittler, L. R., & Anderson, B. J. (Eds.), (2018). *Mercury mercury: The view after messenger*. Cambridge Planetary Science.
- Strom, R. G. (1979). Mercury: A post-mariner 10 assessment. *Space Science Reviews*, *24*(1), 3–70. <https://doi.org/10.1007/BF00221842>
- Thangjam, G., Reddy, V., Le Corre, L., Nathues, A., Sierks, H., Hiesinger, H., et al. (2013). Lithologic mapping of HED terrains on vesta using dawn framing camera color data. *Meteoritics & Planetary Sciences*, *48*(11), 2199–2210. <https://doi.org/10.1111/maps.12132>
- Thomas, R. J., Hynes, B. M., Rothery, D. A., & Conway, S. J. (2016). Mercury's low-reflectance material: Constraints from hollows. *Icarus*, *277*, 455–465. <https://doi.org/10.1016/j.icarus.2016.05.036>
- Thomas, R. J., Rothery, D. A., Conway, S. J., & Anand, M. (2014a). Long-lived explosive volcanism on Mercury. *Geophysical Research Letters*, *41*, 6084–6092. <https://doi.org/10.1002/2014GL061224>
- Thomas, R. J., Rothery, D. A., Conway, S. J., & Anand, M. (2014b). Mechanisms of explosive volcanism on Mercury: Implications from its global distribution and morphology. *Journal of Geophysical Research: Planets*, *119*, 2239–2254. <https://doi.org/10.1002/2014JE004692>

- Vander Kaaden, K. E., McCubbin, F. M., Nittler, L. R., Peplowski, P. N., Weider, S. Z., Frank, E. A., & McCoy, T. J. (2017). Geochemistry, mineralogy, and petrology of boninitic and komatiitic rocks on the mercurian surface: Insights into the mercurian mantle. *Icarus*, *285*, 155–168. <https://doi.org/10.1016/j.icarus.2016.11.041>
- Vilas, F., Domingue, D. L., Helbert, J., D'Amore, M., Maturilli, A., Klima, R. L., et al. (2016). Mineralogical indicators of Mercury's hollows composition in MESSENGER color observations. *Geophysical Research Letters*, *43*(4), 1450–1456. <https://doi.org/10.1002/2015GL067515>
- Weider, S. Z. (2018). Petrology and geochemistry of Mercury. In *Oxford research encyclopedia of planetary science* (p. 127). <https://doi.org/10.1093/acrefore/9780190647926.013.127>
- Weider, S. Z., Nittler, L. R., Murchie, S. L., Peplowski, P. N., McCoy, T. J., Kerber, L., et al. (2016). Evidence from MESSENGER for sulfur- and carbon-driven explosive volcanism on Mercury. *Geophysical Research Letters*, *43*(8), 3653–3661. <https://doi.org/10.1002/2016GL068325>
- Weider, S. Z., Nittler, L. R., Starr, R. D., Crapster-Pregont, E. J., Peplowski, P. N., Denevi, B. W., et al. (2015). Evidence for geochemical terranes on Mercury: Global mapping of major elements with MESSENGER's X-ray spectrometer. *Earth and Planetary Science Letters*, *416*, 109–120. <https://doi.org/10.1016/j.epsl.2015.01.023>
- Wold, S., Esbensen, K., & Geladi, P. (1987). Principal component analysis. *Chemometrics and Intelligent Laboratory Systems*, *2*(1–2), 37–52. [https://doi.org/10.1016/0169-7439\(87\)80084-9](https://doi.org/10.1016/0169-7439(87)80084-9)
- Wright, J., Rothery, D. A., Balme, M. R., & Conway, S. J. (2019). Geology of the Hokusai quadrangle (h05), Mercury. *Journal of Maps*, *15*(2), 509–520. <https://doi.org/10.1080/17445647.2019.1625821>
- Zambon, F., Carli, C., & Altieri, F. (2019). PLANMAP - deliverable D4.2 - Mercury/H05-Hokusai quadrangle spectral parameters maps (final) [Data set]. Zenodo. <https://doi.org/10.5281/zenodo.4772509>
- Zambon, F., Carli, C., & Altieri, F. (2020). PLANMAP - deliverable D4.4 - Mercury/H05-Hokusai quadrangle spectral units map (final) [Data set]. Zenodo. <https://doi.org/10.5281/zenodo.4772274>
- Zuber, M. T., Smith, D. E., Phillips, R. J., Solomon, S. C., Neumann, G. A., Hauck, S. A., et al. (2012). Topography of the northern hemisphere of Mercury from MESSENGER laser altimetry. *Science*, *336*(6078), 217–220. <https://doi.org/10.1126/science.1218805>